

Proton transfer and hydronium formation in ionized water

Ivo S. Vinklársek,^{1,*} Sebastian Trippel,^{1,2} Michal Belina,^{3,4} Luisa Blum,^{1,5}
Hubertus Bromberger,¹ Petr Slavíček,^{3,†} and Jochen Küpper^{1,5,2,‡}

¹Center for Free-Electron Laser Science CFEL, Deutsches

Elektronen-Synchrotron DESY, Notkestr. 85, 22607 Hamburg, Germany

²Center for Ultrafast Imaging, Universität Hamburg, Luruper Chaussee 149, 22761 Hamburg, Germany

³University of Chemical Technologies Prague, Technická 5, 166 28 Prague 6 – Dejvice, the Czech Republic

⁴IT4Innovations, VSB – Technical University of Ostrava, 17. listopadu 2172/15, 708 33 Ostrava, Czech Republic

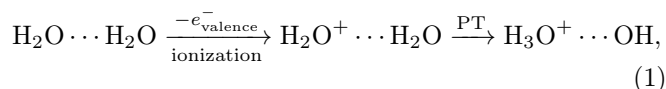
⁵Department of Physics, Universität Hamburg, Luruper Chaussee 149, 22761 Hamburg, Germany

(Dated: 2026-02-20)

Aqueous radiation chemistry emerges through ultrafast proton transfer and ion-radical formation with unexplored energy-redistribution dynamics steering the subsequent reactions. We performed time-resolved disruptive probing on pure water dimer, $(\text{H}_2\text{O})_2$, to disentangle the post-ionization reactions. Through kinetic-energy-resolved ion imaging, we unraveled the dynamics in the $(\text{H}_2\text{O})_2^+$ ground state: at low-energy (~ 0.05 eV) ultrafast proton transfer (~ 19 fs) is followed by $\text{H}_3\text{O}^+ + \text{OH}$ fragmentation (~ 360 fs). At higher energies, proton transfer becomes hindered (~ 60 fs) while the subsequent fragmentation becomes faster (~ 210 fs), evolving into coupled dynamics (> 0.15 eV, ~ 100 fs). Moreover, we observed $(\text{H}_2\text{O})_2^+$ stabilization proceeding through a Zundel-like structure. This reveals how ion-radical formation in ionized hydrogen-bonded networks shapes reactivity in aqueous dynamics.

Radiation chemistry in aqueous environments is largely governed by water radiolysis [1–3]. Upon irradiation, water undergoes a cascade of reactions initiated by the formation of highly reactive ion–radical species [3, 4] that give rise to fundamental phenomena such as biological radiation damage, catalytic transformations, material corrosion, and radical-driven oxidation. A molecular-level characterization of transient reactive species formation and the associated energy redistribution is therefore essential for advancing technologies including radiation therapy [4, 5], wastewater treatment [6, 7], nuclear reactor coolant systems [4, 8], and spaceflight applications [9, 10].

Surprisingly, the initial elementary steps driving the subsequent post-ionization dynamics in water were only recently explored in a time-resolved fashion [2, 3, 11]. These studies provide a coarse picture lacking state- and energy-resolved details. The dominant initial step following valence ionization of liquid water is the ultrafast proton transfer (PT) reaction occurring on a sub-50-fs timescales [3, 12, 13], producing a hydronium cation (H_3O^+) and a hydroxyl radical (OH):



These products drive secondary PTs, oxidative reactions, or undergo recombination. Early pump-probe studies lacked the temporal resolution to capture the initial PT dynamics [12]. Time-resolved x-ray absorption spectroscopy (XAS), enabled by x-ray free-electron lasers, revealed

an ultrafast ~ 46 fs PT event [3], while ultrafast electron diffraction captured $\text{H}_3\text{O}^+ \cdots \text{OH}$ formation in ~ 140 fs followed by the ion–radical separation occurring on a ~ 250 fs timescale [14]. These seemingly different timescales reflect the complementary sensitivities of the probes: XAS probes local electronic structure and diffraction probes atomic motion. Recently, experiments on water-dimer clusters ionized by 24 eV photons reported a PT time of ~ 55 fs, consistent with the earlier XAS results [2].

Molecular clusters permit direct detection of ionic fragments, providing detailed insights into energy redistribution along ultrafast reaction pathways [15], whereas secondary processes characteristic of the bulk liquid [16] remain inaccessible. We used water dimer, $(\text{H}_2\text{O})_2$, a controllable and well-defined model [17–19], to investigate post-ionization chemistry in aqueous systems. Previously, we found a surprising diversity of ion products after single ionization of $(\text{H}_2\text{O})_2$. Our approach using the electrostatic deflector [17, 20] allows the assignment of the originally ionized system without the need for simultaneous detection of multiple ions, as in coincidence-detection methods [2]. Similar to earlier studies [3, 11], we populated $(\text{H}_2\text{O})_2^+$ via strong-field ionization, which raises the question of the initial electronic states. Our recent study showed that ionization predominantly accesses the four energetically lowest states, $D_0 \dots D_3$ [21]. According to our previous *ab initio* simulations [2] these undergo PT, forming the ion–radical complex $(\text{H}_3\text{O} \cdots \text{OH})^+$, which either stabilizes, predominantly for ionization into D_0 , or fragments to $\text{H}_3\text{O}^+ + \text{OH}$.

To explore the elementary dynamics of ionized water dimer, we employed the mass-spectrometric *disruptive-probing* (DP) method. DP was recently presented as a panoramic approach [22] that synchronously monitors delay-dependent signal changes arising from perturbations of evolving electronic and nuclear wavepackets in

* ivo.vinklarek@cfel.de

† petr.slavicek@vscht.cz; URL: <https://photon.vsch.tz/>

‡ jochen.kuepper@cfel.de; URL: <https://www.controlled-molecule-imaging.org>

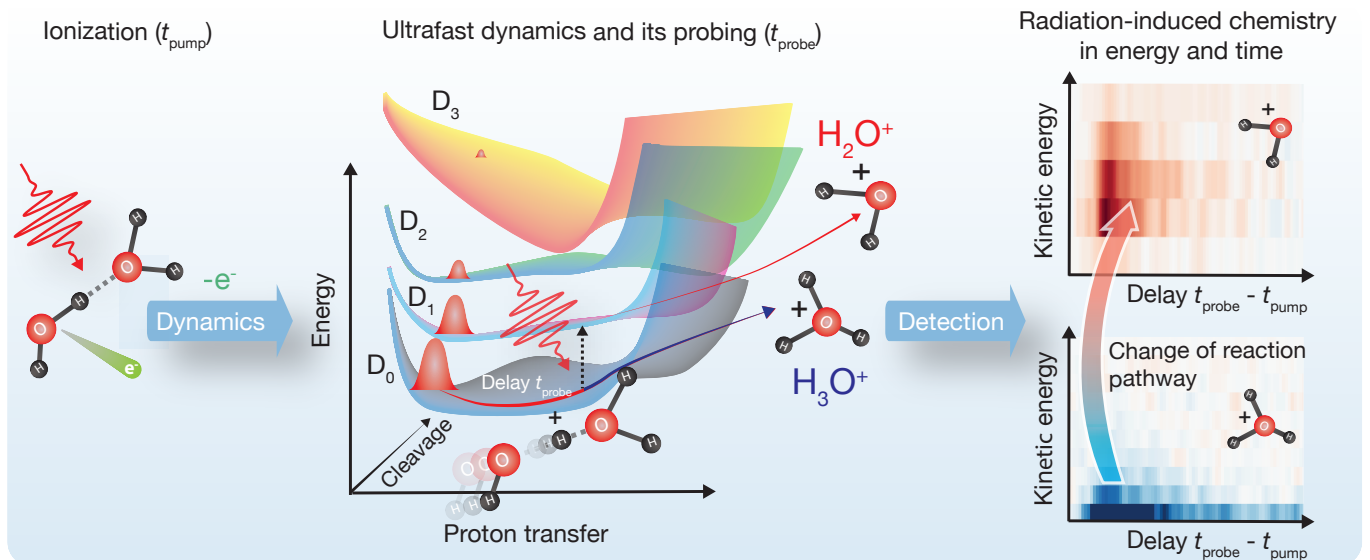


FIG. 1. **Schematic picture of the experiment.** Water dimers were strong-field ionized to launch the ultrafast dynamics. The dynamics were perturbed by a delayed, weak probe pulse that redistributed population and modified the fragmentation pattern. Monitoring all ion species over the pump–probe delay provided time-resolved signatures of PT, ion–radical stabilization, or fragmentation. Velocity-map imaging further yielded delay-dependent momentum distributions that reveal the interplay between PT and fragmentation.

multiple independent photochemical pathways [23]. A schematic overview of the approach is shown in Figure 1: A strong-field ($I_{\text{pump}} = 2.3 \cdot 10^{14} \text{ W/cm}^2$, 800 nm) pump pulse initiates the dynamics, while a weaker, delayed NIR-probe pulse perturbs the ongoing evolution. When temporally separated from the pump, the probe is too weak to induce ionization. Regardless of the precise disruption mechanism [22, 23], the probe modifies the yields of individual ion species as the delay is scanned, thereby encoding the reaction dynamics. So far, DP experiments only took ion yields into account [22]. Our combination of DP with velocity-map imaging (VMI) adds kinetic-energy resolution to the transient ion signals. Complementing these experiments with *ab initio* simulations of the dynamics to 1 ps allowed us to assign fragmentation pathways beyond the initial PT event.

We disentangled the ultrafast dynamics of $(\text{H}_2\text{O})_2^+$ in its electronic ground state, determined energy-resolved timescales for PT (20...100 fs), fragmentation (360...100 fs), and their coalescence at higher energies as well as $(\text{H}_2\text{O})_2^+$ stabilization (~ 1 ps). This directly provides the energy redistribution in the hydronium H_3O^+ , OH radical, and ion-radical formation in ionized aqueous systems.

RESULTS AND DISCUSSION

We recorded transient ion-momentum signals capturing the evolution of the $(\text{H}_2\text{O})_2^+$ reaction pathways, illustrated by selected channels of H_3O^+ and H_2O^+ in Figure 2 A, B and of $(\text{H}_2\text{O})_2^+$ and H^+ in Figure 3 A, B. In the inset of

Figure 2 A, we show an exemplary velocity-map image of H_3O^+ ; the transient signals were extracted from the central regions (yellow circle) using the three-dimensional momentum distributions, thus excluding contributions from $(\text{H}_2\text{O})_2^{2+}$. The strong cross-correlation features peaking at time zero are due to overlap of the pump and probe pulses and not discussed further. All ion species display clear time-dependent behavior at positive pump–probe delays $\Delta t = t_{\text{probe}} - t_{\text{pump}} > 0$. In particular, the $(\text{H}_2\text{O})_2^+$ and H_3O^+ transient signals in Figure 2 A and Figure 3 A, respectively, show a time-dependent bleaching, while all other detected channels exhibit an enhancement of the signal relative to the pump-only level. The total ion yield across all signals, outside the cross-correlation region, remains constant. The DP field perturbs the ongoing fragmentation dynamics in $(\text{H}_2\text{O})_2^+$, resulting in a redistribution of the ion signals across different channels. This redistribution can be tracked by analyzing correlations between the transient signals of individual ion species. Comparing the transient signals with one another reveals that the disruption of H_3O^+ formation enhances the H_2O^+ , OH^+ , and O^+ channels, while the bleached $(\text{H}_2\text{O})_2^+$ signal is transferred to the H^+ channel.

All acquired pump–probe signals were fitted using a parameterized model based on a linear combination of exponentially-modified-Gaussian (EMG) functions shown as red traces in Figure 2 and 3. Model details and extracted parameters for all measured transient signals are given in Materials and Methods and Supplementary Text. While the $(\text{H}_2\text{O})_2^+$, H^+ , and O^+ traces are well described by a single-term EMG model, the other ion species, H_3O^+ , H_2O^+ , and OH^+ , require a double-term EMG model.

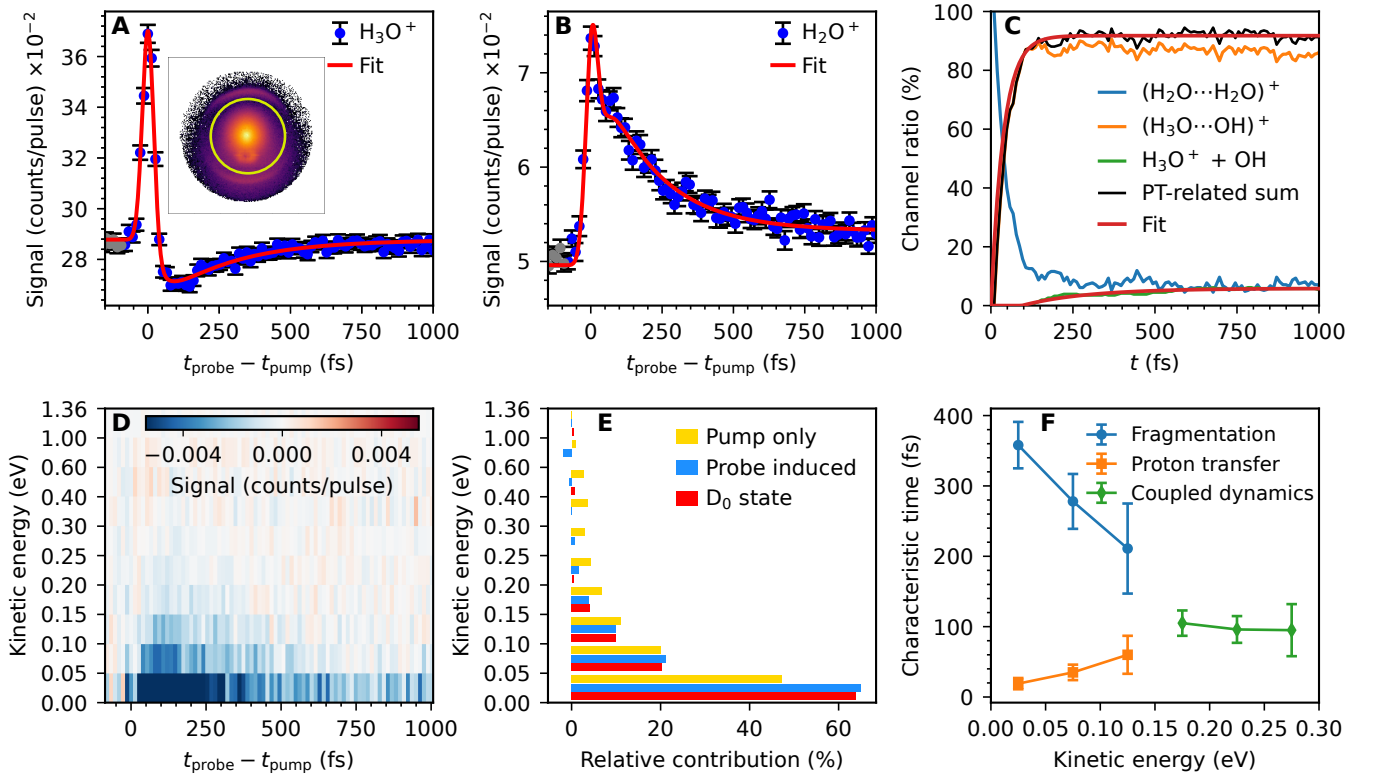


FIG. 2. **Recorded transient signals related to disruptive probing of the H_3O^+ channel and their analysis.** **A** and **B** display transient signals of the H_3O^+ and H_2O^+ channels (blue dots and black error bars), respectively. Fits (red lines) were obtained using the parametric model described in Materials and Methods. The data (gray points) in the range $(-500, -50)$ fs were excluded from the fitting procedure due to probe-induced pre-excitation effects. The inset in **A** shows a velocity map of H_3O^+ with only the central part (yellow circle) originating from $(\text{H}_2\text{O})_2^+$ dynamics. **C** displays the result of simulations of $(\text{H}_2\text{O})_2^+$ dynamics in its ground electronic state (D_0), corresponding data for $D_1 \dots D_3$ are provided in Supplementary Text. **D** represents the background corrected delay- and energy-resolved H_3O^+ signal. **E** shows the comparison of the bleached (blue), pump-only (yellow), and simulated (D_0 , red) kinetic energy distributions [21]. **F** displays the timescales of the H_3O^+ formation obtained from the kinetic energy-resolved analysis using the parametric models described in Materials and Methods; see also Supplementary Text for the individual fits.

Three distinct timescales emerge in the acquired data: The first one represents an ultrafast process of 25... 40 fs, corresponding to the drop in the H_3O^+ trace. A second timescale of several-hundred femtoseconds corresponds to the recovery of the H_3O^+ signal, i. e., 200... 250 fs for H_3O^+ , H_2O^+ , and OH^+ and ~ 580 fs for the O^+ transient. The third timescale, in the $(\text{H}_2\text{O})_2^+$ and H^+ signals, is on the order of 1 ps. The identification of the bleached H_3O^+ and $(\text{H}_2\text{O})_2^+$ channels as the sources of the observed transients ensures that the extracted timescales correspond directly to the H_3O^+ + OH fragmentation and $(\text{H}_2\text{O})_2^+$ stabilization pathways. Thus, the PT and fragmentation dynamics leading to H_3O^+ formation are characterized by lifetimes of 39 ± 9 fs and 250 ± 28 fs. The $(\text{H}_2\text{O})_2^+$ stabilization is largely completed at ~ 1 ps.

The experimental observables were interpreted using *ab initio* calculations using nonadiabatic surface-hopping dynamics at the extended multistate complete-active-space second-order perturbation (XMS-CASPT2) theory level [2]. The simulations, initialized in the $D_0 \dots D_3$

states and extended to 1 ps, provided time-dependent branching ratios of the dominant channels. Figure 2 C illustrates the total yield of $[\text{H}_3\text{O} \dots \text{OH}]^+$ and H_3O^+ products through PT and fragmentation in D_0 . Single-exponential fits (red traces) to the $[\text{H}_3\text{O} \dots \text{OH}]^+$ formation and H_3O^+ fragmentation channels yielded the PT and fragmentation timescales. Overall, we obtained excellent agreement of the simulated PT (38 ± 1 fs) and fragmentation (259 ± 19 fs) timescales with the corresponding experimental timescales derived from the total H_3O^+ signal. In contrast, for the simulated dynamics starting in the excited states $D_1 \dots D_3$, the timescales for PT and fragmentation differ markedly from the experimental ones: For PT the simulations yield 70... 85 fs and for fragmentation they are either considerably slower (D_1 & D_2 , ~ 400 & ~ 725 fs) or faster (D_3 , ~ 200 fs). This is an intriguing finding, as it suggests the selectivity of the DP technique for our experimental conditions. This selectivity might arise from a resonant transition between the D_0 and D_1 states, whose ionization-energy difference closely matches

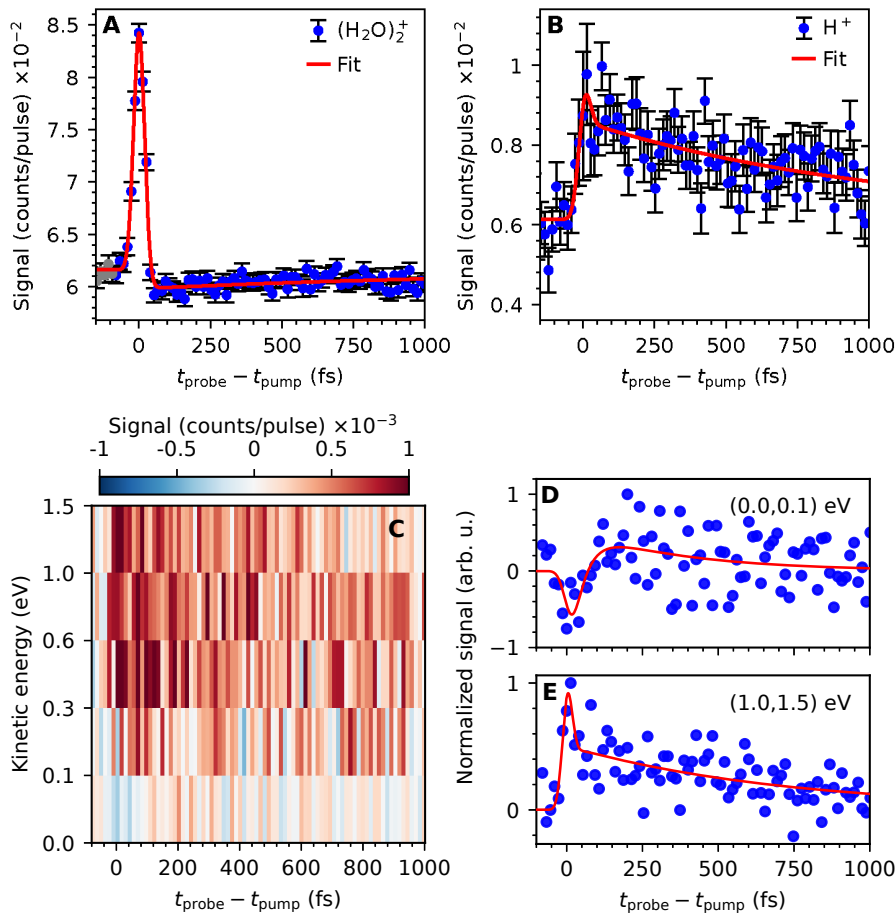


FIG. 3. Recorded transient signals related to disruptive probing of the $(\text{H}_2\text{O})_2^+$ channel. **A** and **B** display transient signals of $(\text{H}_2\text{O})_2^+$ and H^+ , respectively. **C** shows the delay- and energy-resolved H^+ signals after subtraction of the pump-only contributions. **D** and **E** show transient H^+ signals for selected kinetic energy ranges. All fits (red lines) were obtained using the parametric model described in Materials and Methods. The data (gray points) in the range $(-500, -50)$ fs were excluded from the fitting procedure due to probe-induced pre-excitation effects.

the single-photon energy at 800 nm (~ 1.5 eV) as indicated in Figure 1 middle panel.

Energy-resolved chemistry

A kinetic-energy-resolved analysis of the H_3O^+ -formation dynamics yields continuously varying timescales for PT and fragmentation dynamics. The H_3O^+ data were divided in ten kinetic-energy ranges from 0 to 1.36 eV, see Figure 2 D, to which we individually fitted the parametric EMG model. These fits were used for background correction of the recorded energy-resolved data. The resulting delay- and kinetic-energy-resolved H_3O^+ signals are shown in Figure 2 D. A negative signal corresponds to the probe-induced transfer of H_3O^+ population to other fragmentation channels. These signals illustrate the energy-dependence of the chemical dynamics, PT and fragmentation leading to H_3O^+ . The H_3O^+ kinetic-energy redistribution induced by the probe is obtained through integration of these signals along the pump-probe-delay axis.

It shows a vast contribution at kinetic energies < 0.3 eV, see Figure 2 E (blue). This probe-induced kinetic-energy distribution (KED) is clearly different from the observed pump-only H_3O^+ KED (yellow) and in excellent agreement with the H_3O^+ KED obtained from simulations for ionization to the D_0 state of $(\text{H}_2\text{O})_2^+$ (red) [21]. This supports our assignment of observing chemical dynamics in the D_0 state, *vide supra*.

An inspection of Figure 2 D reveals distinct timescales associated with the individual kinetic-energy ranges. The timescales extracted for $0 \dots 0.3$ eV are summarized in Figure 2 F. This shows an increase of the fast-component timescale from 19 fs to 60 fs, associated with PT (orange), with a H_3O^+ kinetic-energy increase from 0 eV up to 0.15 eV. This slowing demonstrates the transition from a direct to a hindered PT process, indicating changes in the energy flow on the potential energy landscape. This is accompanied by a simultaneous decrease of the slow-component, fragmentation, timescale from 358 fs to 211 fs, associated with faster fragmentation at higher energies (blue). At higher kinetic energies, between 0.15 eV and

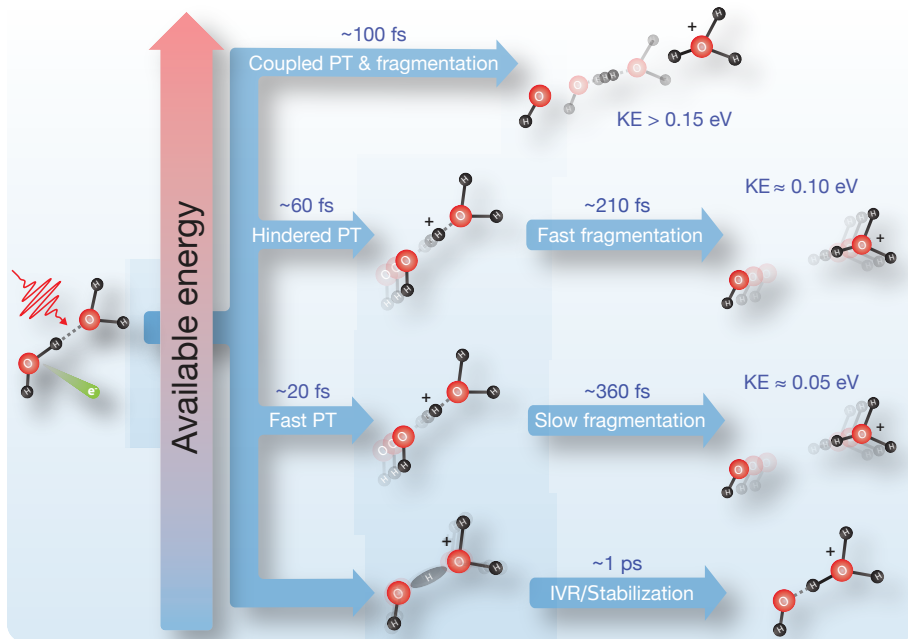


FIG. 4. **The observed $(\text{H}_2\text{O})_2^+$ dynamics.** Energy-resolved PT and fragmentation pathways are identified from the H_3O^+ signal and low-energy stabilization *via* inter-to-intra-molecular vibrational relaxation (IVR) is observed as the $(\text{H}_2\text{O})_2^+$ signal.

0.3 eV, the two timescale converge to ~ 100 fs, obtained from a modified model assuming equal PT and fragmentation timescales. Thus, strikingly, the H_3O^+ formation dynamics exhibits a strong kinetic-energy dependence, with its characteristic timescale changing markedly across the released-energy range, see Figure 4.

Our kinetic-energy-resolved analysis provides insight beyond an electronic-state-averaged description. Interestingly, the higher-energy converged-single-timescale H_3O^+ coincides with the 110 fs delocalized-proton lifetime in aqueous hydroxide solution [24], and it is comparable to the computed period ($\sim 380 \text{ cm}^{-1}/\sim 90 \text{ fs}$) of the $\text{O}\cdots\text{O}$ stretch vibrational mode of $(\text{H}_2\text{O})_2^+$ [25]. The shortening of the $\text{O}\cdots\text{O}$ distance was identified as a key factor governing PT dynamics [26]. We hypothesize that the observed coupled PT and fragmentation dynamics for higher kinetic energies arises from O-O-stretch excitation, leading to vibrationally driven direct dissociation and thus enhanced kinetic-energy release [27]. Such control *via* intermolecular vibrational modes may allow steering the energy carried by hydronium and the OH radical, shaping their roles in radiation chemistry.

Bound-state dynamics

We also observed a signal bleach for the $(\text{H}_2\text{O})_2^+$ transient signal shown in Figure 3 A. The parent ion $(\text{H}_2\text{O})_2^+$ does not have kinetic energy from fragmentation, preventing an kinetic-energy-resolved analysis. Nevertheless, the DP induced the transfer of $(\text{H}_2\text{O})_2^+$ population into the H^+ channel, Figure 3 B. These H^+ signals were an-

alyzed in an energy-resolved manner analogous to the H_3O^+ case, providing the energy-resolved signals of H^+ shown in Figure 3 C. The time-dependent signals for the energy ranges $0 \dots 0.1 \text{ eV}$ and $1.0 \dots 1.5 \text{ eV}$ are shown in Figure 3 E. The H^+ signal in the $0 \dots 0.1 \text{ eV}$ range shows a rapid signal bleach in the first 100 fs, the origin of which remains unresolved. Most H^+ appear with kinetic energies of $0.3 \dots 1.5 \text{ eV}$, with a timescale of $0.7 \dots 1.4 \text{ ps}$. We ascribe the H^+ signal to the disruption of transient, non-stabilized $(\text{H}_2\text{O})_2^+$ and thus the observed picosecond timescale to $(\text{H}_2\text{O})_2^+$ stabilization, as illustrated in Figure 4.

However, in the isolated H_2O and OH radicals, O-H covalent bonds have dissociation energies of about 5.1 eV and 4.4 eV, respectively [28, 29]. Cleaving such bonds would require the absorption of three to four 800 nm photons. The O-H bonds in isolated H_3O^+ are even stronger [30]. Even though the hydronium-ion-hydroxyl-radical pair, like Zundel complexes, has a strong proton delocalization along its O-O axis [31], the proton is overall still strongly bound. Consequently, our weak probing pulse cannot drive the stabilized ion-radical $(\text{H}_2\text{O})_2^+$ pair into the proton channel.

We assume that the weak probe pulse can eject the proton only during the early stage of the dynamics, before the reaction energy is redistributed from intermolecular modes, e.g., proton-shuttling and O-O stretch, to intramolecular modes to form a stabilized $(\text{H}_2\text{O})_2^+$. In other words, the dynamics observed on the hundreds-of-femtoseconds to picosecond timescale are attributed to the decay of transient Zundel-like $(\text{H}_2\text{O})_2^+$, ultimately leading to the formation of a stabilized ion-radical pair

$\text{H}_3\text{O}^+ \cdots \text{OH}$. In the liquid, Zundel-like structures decay substantially faster (100–200 fs) [24, 32]. Nevertheless, these sub-200 fs components mainly represent localized proton fluctuations caused by short-lived structural rearrangements, rather than a stable, fully formed Zundel configuration, which persists for much longer times (>480 fs) [33].

A remaining open question concerns the electronic-state contribution to the observed stabilization dynamics of $(\text{H}_2\text{O})_2^+$. Based on Ammosov-Delone-Krainov tunneling-ionization calculations [21], the majority of the $(\text{H}_2\text{O})_2^+$ signal detected in the pump-only experiment [17] originates from the D_0 and D_1 states. However, unlike the assignment of the H_3O^+ dynamics to the D_0 state (*vide supra*), the $(\text{H}_2\text{O})_2^+$ signals cannot be uniquely attributed to a single electronic state. A definitive assignment requires further analysis beyond the scope of the present work.

Overall, we unraveled the initial processes after ionization of water exploiting the $(\text{H}_2\text{O})_2^+$ system, with a focus on the appearance of the primary ionic products, including hydronium ion (H_3O^+) and stabilized $(\text{H}_2\text{O})_2^+$. Utilizing the energy distributions of the reaction products, our results go beyond electronic-state-averaged descriptions. As illustrated in Figure 4, low-energy stabilization of $(\text{H}_2\text{O})_2^+$ on picosecond timescales proceeds through Zundel-like configurations that stabilize by atomic rear-

angement and vibrational relaxation from intermolecular to intramolecular modes. For increasing energies, we see an energy-driven evolution from sequential ultrafast proton transfer with subsequent fragmentation of the ion-radical pair to an intermediate-timescale concerted pathway.

Our results demonstrate that combining species-controlled samples, multi-mass velocity-map imaging, and disruptive probing with computational-dynamics simulations allows us to disentangle the ultrafast dynamics of complex molecular systems in energy and time. The agreement of our energy-averaged data with earlier ultrafast post-ionization dynamics observed in clusters [2] and liquids [3] demonstrates that our observations are directly relevant to initial-stage liquid-phase chemistry. The sensitivity to internal dynamics, such as the inferred Zundel-like structures, provides opportunities for the investigation of internal motions including general isomerizations. Our approach further opens important prospects for probing biomolecules in their native aqueous environment [34]. Coincidence measurements combining the ion imaging with electron spectroscopy offer direct access to the coupled dynamics of nuclear and electronic reaction pathways. This provides a basis for future attempts to tailor wavepackets to steer ion-radical chemistry in aqueous environments.

-
- [1] E. Alizadeh and L. Sanche, Precursors of solvated electrons in radiobiological physics and chemistry, *Chem. Rev.* **112**, 5578 (2012).
- [2] K. Schnorr, M. Belina, S. Augustin, H. Lindenblatt, Y. Liu, S. Meister, T. Pfeifer, G. Schmid, R. Treusch, F. Trost, P. Slavíček, and R. Moshhammer, Direct tracking of ultrafast proton transfer in water dimers, *Sci. Adv.* **9**, eadg7864 (2023).
- [3] Z.-H. Loh, G. Doumy, C. Arnold, L. Kjellsson, S. H. Southworth, A. Al Haddad, Y. Kumagai, M.-F. Tu, P. J. Ho, A. M. March, R. D. Schaller, M. S. Bin Mohd Yusof, T. Debnath, M. Simon, R. Welsch, L. Inhester, K. Khalili, K. Nanda, A. I. Krylov, S. Moeller, G. Coslovich, J. Koralek, M. P. Minitti, W. F. Schlotter, J.-E. Rubensson, R. Santra, and L. Young, Observation of the fastest chemical processes in the radiolysis of water, *Science* **367**, 179 (2020).
- [4] B. C. Garrett, D. A. Dixon, D. M. Camaioni, D. M. Chipman, M. A. Johnson, C. D. Jonah, G. A. Kimmel, J. H. Miller, T. N. Rescigno, P. J. Rossky, S. S. Xantheas, S. D. Colson, A. H. Laufer, D. Ray, P. F. Barbara, D. M. Bartels, K. H. Becker, K. H. Bowen, S. E. Bradforth, I. Carmichael, J. V. Coe, L. R. Corrales, J. P. Cowin, M. Dupuis, K. B. Eisenthal, J. A. Franz, M. S. Gutowski, K. D. Jordan, B. D. Kay, J. A. LaVerne, S. V. Lyman, T. E. Madey, C. W. McCurdy, D. Meisel, S. Mukamel, A. R. Nilsson, T. M. Orlando, N. G. Petrik, S. M. Pimblott, J. R. Rustad, G. K. Schenter, S. J. Singer, A. Tokmakoff, L.-S. Wang, , and T. S. Zwier, Role of water in electron-initiated processes and radical chemistry: Issues and scientific advances, *Chem. Rev.* **105**, 355 (2005).
- [5] C. D. Jonah, A short history of the radiation chemistry of water, *Radiat. Res.* **144**, 141 (1995).
- [6] L. Jiang and H. Iwahashi, Current research on high-energy ionizing radiation for wastewater treatment and material synthesis, *Environmental Progress & Sustainable Energy* **39**, 13294 (2020).
- [7] L. Wojnárovits and E. Takács, Wastewater treatment with ionizing radiation, *Journal of Radioanalytical and Nuclear Chemistry* **311**, 973 (2017).
- [8] H. Christensen and S. Sunder, Current state of knowledge of water radiolysis effects on spent nuclear fuel corrosion, *Nuclear Technology* **131**, 102 (2000).
- [9] Y.-Z. Fang, S. Yang, and G. Wu, Free radicals, antioxidants, and nutrition, *Nutrition* **18**, 872 (2002).
- [10] F. E. Garrett-Bakelman, M. Darshi, S. J. Green, R. C. Gur, L. Lin, B. R. Macias, M. J. McKenna, C. Meydan, T. Mishra, J. Nasrini, B. D. Piening, L. F. Rizzardi, K. Sharma, J. H. Siamwala, L. Taylor, M. H. Vitaterna, M. Afkarian, E. Afshinnekoo, S. Ahadi, A. Ambati, M. Arya, D. Bezdán, C. M. Callahan, S. Chen, A. M. K. Choi, G. E. Chlipala, K. Contrepois, M. Covington, B. E. Crucian, I. De Vivo, D. F. Dinges, D. J. Ebert, J. I. Feinberg, J. A. Gandara, K. A. George, J. Goutsias, G. S. Grills, A. R. Hargens, M. Heer, R. P. Hillary, A. N. Hoofnagle, V. Y. H. Hook, G. Jenkinson, P. Jiang, A. Keshavarzian, S. S. Laurie, B. Lee-McMullen, S. B. Lumpkins, M. MacKay, M. G. Maienschein-Cline, A. M. Melnick, T. M. Moore, K. Nakahira, H. H. Patel, R. Pietrzyk, V. Rao, R. Saito, D. N. Salins, J. M. Schilling, D. D. Sears,

- C. K. Sheridan, M. B. Stenger, R. Tryggvadottir, A. E. Urban, T. Vaisar, B. Van Espen, J. Zhang, M. G. Ziegler, S. R. Zwart, J. B. Charles, C. E. Kundrot, G. B. I. Scott, S. M. Bailey, M. Basner, A. P. Feinberg, S. M. C. Lee, C. E. Mason, E. Mignot, B. K. Rana, S. M. Smith, M. P. Snyder, and F. W. Turek, The nasa twins study: A multidimensional analysis of a year-long human spaceflight, *Science* **364**, eaau8650 (2019).
- [11] S. Li, L. Lu, S. Bhattacharyya, C. Pearce, K. Li, E. T. Nienhuis, G. Doumy, R. D. Schaller, S. Moeller, M.-F. Lin, G. Dakovski, D. J. Hoffman, D. Garratt, K. A. Larsen, J. D. Koralek, C. Y. Hampton, D. Cesar, J. Duris, Z. Zhang, N. Sudar, J. P. Cryan, A. Marinelli, X. Li, L. Inhester, R. Santra, and L. Young, Attosecond-pump attosecond-probe x-ray spectroscopy of liquid water, *Science* **383**, 1118 (2024).
- [12] O. Marsalek, C. G. Elles, P. A. Pieniazek, E. Pluhařová, J. VandeVondele, S. E. Bradforth, and P. Jungwirth, Chasing charge localization and chemical reactivity following photoionization in liquid water, *J. Chem. Phys.* **135**, 224510 (2011).
- [13] E. Kamarchik, O. Kostko, J. M. Bowman, M. Ahmed, and A. I. Krylov, Spectroscopic signatures of proton transfer dynamics in the water dimer cation, *J. Chem. Phys.* **132**, 194311 (2010).
- [14] M.-F. Lin, N. Singh, S. Liang, M. Mo, J. P. F. Nunes, K. Ledbetter, J. Yang, M. Kozina, S. Weathersby, X. Shen, A. A. Cordones, T. J. A. Wolf, C. D. Pemmaraju, M. Ihme, and X. J. Wang, Imaging the short-lived hydroxyl-hydronium pair in ionized liquid water, *Science* **374**, 92 (2021).
- [15] I. S. Vinklársek, J. Suchan, J. Rakovský, K. Moriová, V. Poterya, P. Slavíček, and M. Fárnik, Energy partitioning and spin-orbit effects in the photodissociation of higher chloroalkanes, *Phys. Chem. Chem. Phys.* **23**, 14340 (2021).
- [16] M. J. Goodwin, J. C. Dickenson, A. Ripak, A. M. Deetz, J. S. McCarthy, G. J. Meyer, and L. Troian-Gautier, Factors that impact photochemical cage escape yields, *Chem. Rev.* **124**, 7379 (2024).
- [17] I. S. Vinklársek, H. Bromberger, N. Vadassery, W. Jin, J. Küpper, and S. Trippel, Reaction pathways of water dimer following single ionization, *J. Phys. Chem. A* **128**, 1593 (2024), arXiv:2308.08006 [physics].
- [18] H. Bieker, J. Onvlee, M. Johnny, L. He, T. Kierspel, S. Trippel, D. A. Horke, and J. Küpper, Pure molecular beam of water dimer, *J. Phys. Chem. A* **123**, 7486 (2019), arXiv:1904.08716 [physics].
- [19] E. Vogt and H. G. Kjaergaard, Vibrational spectroscopy of the water dimer at jet-cooled and atmospheric temperatures, *Annu. Rev. Phys. Chem.* **73**, 209 (2022).
- [20] Y.-P. Chang, D. A. Horke, S. Trippel, and J. Küpper, Spatially-controlled complex molecules and their applications, *Int. Rev. Phys. Chem.* **34**, 557 (2015), arXiv:1505.05632 [physics].
- [21] I. Vinklársek, M. Belina, H. Bromberger, Á. C. Fernandez, S. Trippel, P. Slavíček, and J. Küpper, (2025), in preparation.
- [22] B. Jochim, L. DeJesus, and M. Dantus, Ultrafast disruptive probing: Simultaneously keeping track of tens of reaction pathways, *Rev. Sci. Instrum.* **93**, 033003 (2022).
- [23] B. J. Sussman, D. Townsend, M. Y. Ivanov, and A. Stolow, Dynamic stark control of photochemical processes, *Science* **314**, 278 (2006).
- [24] S. T. Roberts, P. B. Petersen, K. Ramasesha, A. Tokmakoff, I. S. Ufimtsev, and T. J. Martinez, Observation of a zundel-like transition state during proton transfer in aqueous hydroxide solutions, *Proc. Natl. Acad. Sci. U.S.A.* **106**, 15154 (2009).
- [25] J. J. Talbot, X. Cheng, J. D. Herr, and R. P. Steele, Vibrational signatures of electronic properties in oxidized water: unraveling the anomalous spectrum of the water dimer cation, *J. Am. Chem. Soc.* **138**, 11936 (2016).
- [26] O. Svoboda, D. Hollas, M. Ončák, and P. Slavíček, Reaction selectivity in an ionized water dimer: Nonadiabatic ab initio dynamics simulations, *Phys. Chem. Chem. Phys.* **15**, 11531 (2013).
- [27] K. Grygoryeva, J. Rakovský, I. Vinklársek, O. Votava, M. Fárnik, , and V. Poterya, Vibrationally mediated photodissociation dynamics of pyrrole, *AIP Adv.* **9**, 0351511 (2019).
- [28] P. Maksyutenko, T. R. Rizzo, and O. V. Boyarkin, A direct measurement of the dissociation energy of water, *J. Chem. Phys.* **125**, 181101 (2006).
- [29] B. Ruscic, A. F. Wagner, L. B. Harding, R. L. Asher, D. Feller, D. A. Dixon, K. A. Peterson, Y. Song, X. Qian, C.-Y. Ng, J. Liu, W. Chen, and D. W. Schwenke, On the enthalpy of formation of hydroxyl radical and gas-phase bond dissociation energies of water and hydroxyl, *J. Phys. Chem. A* **106**, 2727 (2002).
- [30] A. Bodi, J. Csontos, M. Kállay, S. Borkar, and B. Sztáray, On the protonation of water, *Chemical Science* **5**, 3057 (2014).
- [31] O. Vendrell, F. Gatti, and H.-D. Meyer, Full dimensional (15-dimensional) quantum-dynamical simulation of the protonated water dimer. ii. infrared spectrum and vibrational dynamics, *J. Chem. Phys.* **127**, 10.1063/1.2787596 (2007).
- [32] S. Woutersen and H. J. Bakker, Ultrafast vibrational and structural dynamics of the proton in liquid water, *Phys. Rev. Lett.* **96**, 138305 (2006).
- [33] M. Thämer, L. De Marco, K. Ramasesha, A. Mandal, and A. Tokmakoff, Ultrafast 2d ir spectroscopy of the excess proton in liquid water, *Science* **350**, 78 (2015).
- [34] J. Onvlee, S. Trippel, and J. Küpper, Ultrafast light-induced dynamics in the microsolvated biomolecular indole chromophore with water, *Nat. Commun.* **13**, 7462 (2022), arXiv:2103.07171 [physics].

ACKNOWLEDGMENTS

Funding: This work was supported by Deutsches Elektronen-Synchrotron (DESY), a member of the Helmholtz Association (HGF), and by the Cluster of Excellence “Advanced Imaging of Matter” of the Deutsche Forschungsgemeinschaft (DFG, AIM, EXC 2056, ID 390715994). Data processing and analysis were carried out using the Maxwell computing resources at DESY. The endstation for controlled-molecule experiments (eCOMO) was funded with support from the Center for Molecular Water Science. I.S.V. acknowledges support from the Alexander von Humboldt Foundation. M.B. and P.S. thank to Czech Science foundation (projects numbers 23-07066S and 26-22810S).

Author contributions: Original concept: I.S.V., J.K.; Performed experiments: I.S.V., L.B.; Analysis of data: I.S.V. Trajectory based simulations: M.B., P.S.; Software and experimental support: H.B.; Original draft: I.S.V.; Discussion: I.S.V., S.T., M.B., P.S., J.K.; Writing and editing: I.S.V., S.T., P.S., J.K.;

Competing interests: There are no competing interests to declare.

Data and materials availability: All data underlying the figures and all analysis scripts are provided as Supplementary Material. All processed data are publicly available at Zenodo (DOI: 10.5281/zenodo.18678891, link). All raw data are archived in DESY's data repositories

under ID 11019141 and are available upon reasonable request.

Supplementary materials

Materials and Methods
Supplementary Text
Tutorial on disruptive probing
Figures SI1 to SI31
Tables SI1 to SI4
References (1-27)

Supplementary information: Proton transfer and hydronium formation in ionized water

Ivo S. Vinklárek,^{1,*} Sebastian Trippel,^{1,2} Michal Belina,^{3,4} Luisa Blum,^{1,5}
Hubertus Bromberger,¹ Petr Slavíček,^{3,†} and Jochen Küpper^{1,5,2,‡}

¹*Center for Free-Electron Laser Science CFEL, Deutsches*

Elektronen-Synchrotron DESY, Notkestr. 85, 22607 Hamburg, Germany

²*Center for Ultrafast Imaging, Universität Hamburg, Luruper Chaussee 149, 22761 Hamburg, Germany*

³*University of Chemical Technologies Prague, Technická 5, 166 28 Prague 6 – Dejvice, the Czech Republic*

⁴*IT4Innovations, VSB – Technical University of Ostrava, 17. listopadu 2172/15, 708 33 Ostrava, Czech Republic*

⁵*Department of Physics, Universität Hamburg, Luruper Chaussee 149, 22761 Hamburg, Germany*

(Dated: 2026-02-20)

This PDF file includes:

Materials and Methods

Supplementary Text

Tutorial on disruptive probing

Figs. S1 to S31

Tables S1 to S4

References (1-27)

* ivo.vinklarek@cfel.de

† petr.slavicek@vscht.cz; URL: <https://photox.vscht.cz/>

‡ jochen.kuepper@cfel.de; URL: <https://www.controlled-molecule-imaging.org>

SI1. MATERIALS AND METHODS

A. Experimental methods and data analysis

1. Preparation of water dimer ensemble

All the experiments were performed using the endstation for controlled molecule (eCOMO) experiments [1]. A molecular beam containing water clusters was generated by supersonic expansion of water mixture with helium buffer gas ($p_{\text{He}} = 100$ bar) using an Even-Lavie valve [2] running at 100 Hz repetition rate and stabilized at a temperature of 50 °C. The expanded gas was then skimmed by the first skimmer (= 3 mm) into the deflector chamber, where it was further collimated by a second skimmer (= 1.5 mm) before entering the electrostatic deflector. The inhomogeneous electrostatic field ($E_d \sim 100$ kV/cm, $U_d = 22$ kV) resulted in spatial dispersion of the various water clusters according to their effective dipole-moment-to-mass ratios [3]. Behind the deflector, the molecular beam was further cut by the knife edge to improve separation of the various water clusters [4]. The estimated purity of the water dimer beam was around 96%. Finally, the molecular beam was introduced to a VMI chamber by the third skimmer (= 1.5 mm) and was crossed with the IR laser radiation at the interaction center of the VMI spectrometer with a perpendicular geometry towards the molecular beam velocity direction [5]. Interaction of the IR laser with the deflected water dimer particles caused their ionization, which then enabled the ionized particles extraction towards the detector. The ion products were imaged by the combination of microchannel plates in Z-stack ($U_{\text{MCP}} = -2.4$ kV) and phosphor screen (P47, $U_{\text{PS}} = 4.3$ kV), which scintillated the ion signal into the flashes recorded by the ultrafast Timepix3 camera with a temporal resolution of 1.7 ns [6]. The precise ion signal time-of-flight recording enabled us to reconstruct the 3D momentum Newton sphere for each detected ion signal. The data were processed using PymePix software [7, 8]. To resolve the physical events, we used a clustering and centroiding algorithm to retrieve the time of flight and impact position of each ion.

2. Disruptive probing

The disruptive probing pump-probe scheme was applied to study the cluster fragmentation after its single ionization [9]. First a strong ionizing pulse at 800 nm (peak intensity $I_{\text{pump}} = 2.3 \cdot 10^{14}$ W/cm², temporal width $\sigma^{\text{pump}} = 18.9$ fs, and Keldysh parameter $\gamma_K = 0.65$, linear polarization) triggered the dynamics followed by a second weaker probing pulse at 800 nm ($I_{\text{probe}} = 0.4 \cdot 10^{14}$ W/cm², $\sigma_{\text{FWHM}}^{\text{probe}} = 18.9$ fs) with a temporal delay τ . The pulses were cross-polarized, with the pump pulse p-polarized (parallel with the detector plane) and the probe pulse s-polarized. The intensity of the second probing pulse was

set such that no ions were observed from the probe-only data acquisition. The purpose of the second pulse was to cause disruption of the ongoing water dimer dynamics, resulting in a change in the resulting ion yields, which were then measured as a function of the pump-probe delay.

3. Scheme of disruptive probing setup

In Figure SII1, there is shown a schematic picture of the pump-probe setup for the disruptive probing technique. The Astrella laser (Coherent) seeded with the Vitara laser (Coherent) and pumped by the Nd:YAG laser provides 45 fs laser pulses at 800 nm, which intensity is controlled by a combination of a half-waveplate and a thin film polarizer. Next, the beam is split into two paths, i.e., pump beam path, which leads directly to the endstation for Controlled Molecule experiments (eCOMO), and probe beam path, which leads through the delay stage and telescope. Both beams are then coupled again on the second beamsplitter and focused by 75 mm lens into the experimental chamber. The telescope is used to compensate for any optical errors in aligning the pump and probe focus positions.

4. Parametric modeling of acquired time-resolved signal using disruptive probing

The response of the targeted ion to the probing field is observed via the time-dependent change in ion yields of individual ion species. This was shortly discussed in [9], and we provide a broadened tutorial of the empirical description of the effects caused by disruptive probing in Section SI3.

To investigate the original dynamics, we apply the generalized model for fitting the pump-probe signals build from: (1) A Gaussian g , representing the cross-correlation ion signal. (2) An exponentially modified Gaussian function (EMG), representing the sought ionic dynamics broadened by the instrumental response function (IRF). (3) An error-function step θ , describing either signal originating in the probe-induced secondary fragmentation of the relaxed ions, or signal originating in probe-only ionization of pump-pre-excited water dimer. (4) A constant $[\text{Ch}^+]_0$, representing the pump-only signal level.

For each specific ion channel Ch^+ , we model the obtained transient signal as

$$\begin{aligned}
 & [\text{Ch}^+] \left(t; a_{\text{IRF}}, \sigma_{\text{IRF}}, \{a_k\}, \{\tau_k\}, a_\theta, [\text{Ch}^+]_0 \right) \\
 & = g(t; a_{\text{IRF}}, \sigma_{\text{IRF}}) + \sum_k \text{EMG}_k(t; a_k, \tau_k, \sigma_{\text{IRF}}) \quad (\text{SII}) \\
 & + \theta(t; a_\theta, \sigma_{\text{IRF}}) + [\text{Ch}^+]_0,
 \end{aligned}$$

where a_{IRF}/θ and σ_{IRF} denote the amplitudes and the width of the applied functions, respectively, and the in-

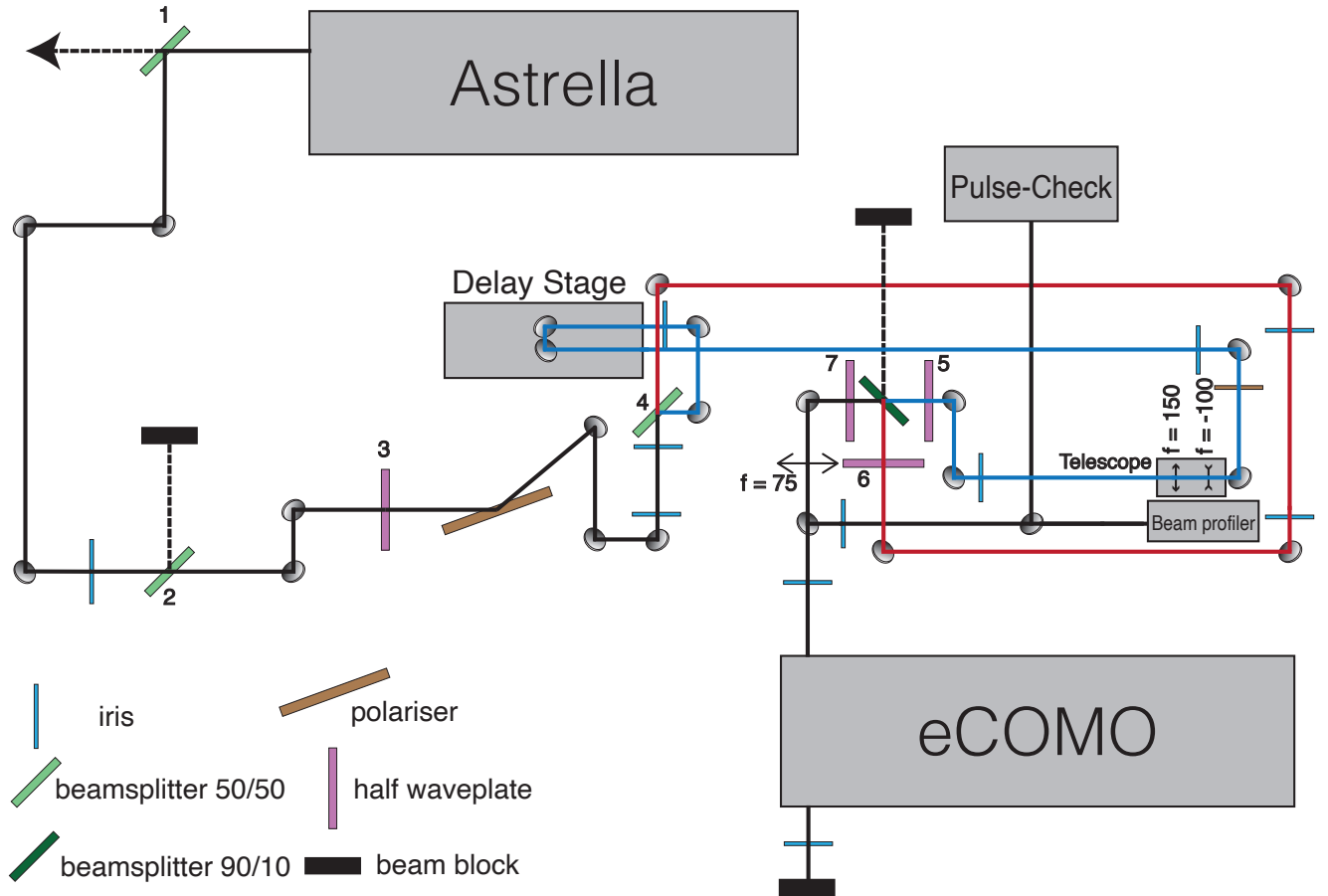


FIG. S11. Schematic picture of the pump-probe setup used for the disruptive probing experiment.

dividual elements in the sets $\{a_k\}$ and $\{\tau_k\}$ express the amplitudes and characteristic times describing the ion dynamics. Notice that all the fitted parameters are channel-specific. We added an additional constraint of an upper limit for the σ_{IRF} equal to $\sigma_{\text{IRF}}^{\text{max}} = 20.7$, which we obtained from fitting the cross-correlation signal of all detected ions, see also Section S11 A 5.

Finally, some of the signal dependencies exhibit a double-exponential character, which is characteristic of processes involving the initial population followed by the decay of a metastable state. In such cases, we impose an additional constraint on the amplitudes a_k and decay times τ_k in the form

$$\frac{a_1}{\tau_1} = -\frac{a_2}{\tau_2}. \quad (\text{SI2})$$

This condition is derived from an assumption that the final ion product is populated from a metastable state. A detailed derivation of this constraint is provided in Section S12 H.

In the special case of converging lifetimes, i. e., when $\tau_1 - \tau_2 \rightarrow 0$, fitting the data with a two-component EMG model becomes unfeasible due to ill-defined amplitudes. In this limit, the second term in Equation S11 is replaced

by the convolution of the normalized Gaussian excitation function g with a causal gamma-like response function

$$a \cdot \left[g(t'; \sigma_{\text{IRF}}) * \left(\frac{t'}{\tau} e^{-t'/\tau} \cdot \Theta(t') \right) \right] (t). \quad (\text{SI3})$$

5. Estimation of time zero and laser pulse duration

In the case of fitting the individual ion channel signals, we applied the same non-varying value for the position of the zero pump-probe delay t_0 . The value was obtained from fitting a Gaussian function and a step function to the all-ion signal after subtraction of the background signal; see Figure S12. The obtained value of t_0^{All} is equal to 1.09(99).

Secondly, we wanted to estimate upper limit of width σ_{IRF} characterizing the broadening of observed molecular dynamics due to durations of pump and probe pulses. The reason for applying a maximum value for σ_{IRF} rather than σ_{IRF} as a non-varying parameter comes from the fact that individual ion channels may originate from higher excited levels of $(\text{H}_2\text{O})_2^+$, and therefore their actual σ_{IRF}

values could be narrower. On the contrary, a significant broadening of the function width over the upper limit of σ_{IRF} indicates underlying dynamics with a rate constants on similar timescale as the IRF. We obtained upper limit for σ_{IRF} from the fitting of all ion signal, equal to $\sigma_{\text{IRF}}^{\text{All}} = 20.7(8)$ fs, which characterizes the broadening caused by the pump and probe pulse durations. Independently, we estimate the value of σ_{IRF} using an autocorrelator (PulseCheck, APE). Assuming a Gaussian temporal shape, the FWHM of the laser pulse is 44.5 fs corresponding to $\sigma_{\text{IRF}}^{\text{AC}} = 18.9(1.0)$ fs. Both values are in a reasonable agreement. As the estimated σ_{IRF} should be applied as an upper limit in analysis of individual ion signal, we selected to apply $\sigma_{\text{IRF}}^{\text{max}} = 20.7(8)$ fs for the fitting.

In perfect conditions of the disruptive probing experiment, we would expect the signal levels to be the same on the left and right sides of the cross-correlation signal. We observe only a very small increase in the signal at positive pump-probe delays, which is caused by probe laser ionization. Therefore, we can be confident that this does not cause any uncertainty regarding the origin of the measured signals for the main channels.

6. Probe laser focus

The checking of the probe beam focus by a laser-beam profiler (CinCam CMOS-1201-Nano, CINOGY) revealed a secondary ring structure; see the image taken and plotted in logarithmic scale in Figure SI3. This was found to be caused by diffraction on the second beamsplitter, which couples the pump and probe beams before focusing them into the velocity map imaging (VMI) chamber. Therefore, we integrated the signal in the ring and center areas of the focus to calculate a correction factor for the estimated laser field intensity caused by the probing pulse. The correction factor was estimated to be 0.7.

The focus of the pumping laser was also checked and showed a nicely Gaussian profile without any diffraction pattern.

B. Trajectory simulations

We investigated the dynamics of the water dimer following ionization into four different electronic states, D_0 – D_3 , over a time window of up to 1 ps. These ionized states were generated by removing an electron from the $1b_1$ - and $3a_1$ -like molecular orbitals. Compared to previous the study [10] using the same method, we expanded the simulations by increasing the number of trajectories from about one hundred to four hundred. The dynamics were treated using the nonadiabatic surface-hopping approach in the fewest switches formulation [11]. The electronic structure of the singly ionized dimer was described using the extended multistate complete active space second-order perturbation theory (XMS-CASPT2) [12] with an active space of 11 electrons in 6 molecular orbitals. For

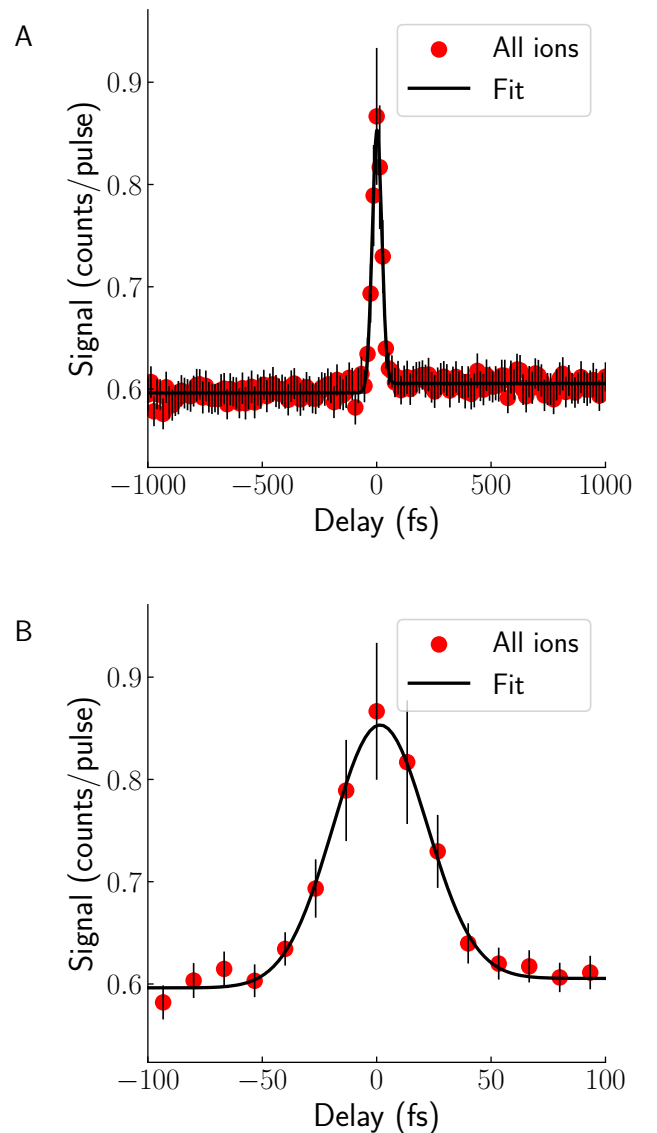


FIG. SI2. (A) Fitting of t_0 and σ_{IRF} from the integrated all ion signal resulting in 1.36(84) fs and 21.2(8) fs, respectively. (B) Zoomed-in plot at (-100,100) fs range.

these calculations, the cc-pVDZ basis set was employed. All electronic structure computations were performed with the BAGEL program, version 1.2.0 [12]. Nuclear motion was propagated using a Verlet algorithm with a time step of 4 atomic units (a.u.), ~ 0.1 fs.

The starting conditions for the non-adiabatic molecular dynamics (NAMMD) simulations were generated from molecular dynamics (MD) employing a quantum thermostat based on the generalized Langevin equation (GLE) [13, 14]. This approach incorporates nuclear quantum effects into both, atomic positions and momenta. A temperature of 180 K was used, together with GLE parameters $\hbar\omega/kT = 50$ and $N_s = 50$. Thermostat matrices were downloaded from the GLE4MD repository [13, 14]. The MD simulations were run with a time step of 20 a.u.

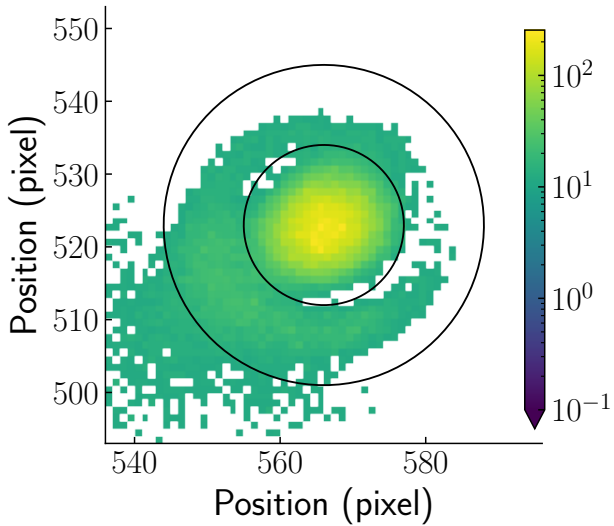


FIG. S13. Image of the probe beam laser focus taken by the laser-beam profiler. It is shown with the logarithmic scale of the intensity axis.

(~ 0.48 fs) and a total duration length of 50 ps. Energies and gradients were obtained with the Boese-Martin for kinetics (BMK) functional [15] in combination with the 6-31++g** basis set, as implemented in the Gaussian09, revision D.01 [16]. Initial geometries and velocities were extracted using a fixed time interval. The propagation of the equations of motion was carried out with the in-house ABIN package, version 1.1 [17].

The NAMD analysis was first based exclusively on nuclear positions. Once dissociation was observed, the charge distribution on the fragments was determined, and if a fragment carried a charge of +1, its center-of-mass kinetic energy was evaluated. Mulliken charge population analyses were performed for every 100th geometry along each trajectory, using the Complete Active Space Self-Consistent Field (CASSCF) method with 11 electrons in 6 active orbitals and the 6-31+g* basis set. These electronic structure and charge calculations were carried out with MOLPRO, version 2015.1 [18, 19].

1. Parametric model for description of simulated channel dynamic

To characterize the timescales of ion-pair $\text{H}_3\text{O}^+\cdots\text{OH}$ formation and subsequent fragmentation, we employed a single-exponential kinetic model [10]:

$$[\text{P}](t) = a_{\text{P}} \cdot \left[1 - \exp\left(-\frac{t-t_0}{\tau_{\text{P}}}\right) \right], \quad (\text{SI4})$$

where a_{P} is a scaling amplitude and τ_{P} is the characteristic time of the investigated process P. For PT, we denote the lifetime as τ_{PT} , and for fragmentation, as $\tau_{\text{H}_3\text{O}^+}$. Finally, the retardation t_0 arises from the methodology applied

in *ab initio* simulations, where the identification of the ion-radical pair $[\text{H}_3\text{O}\cdots\text{OH}]^+$ and its subsequent fragmentation into H_3O^+ is based on geometrical constraints involving interatomic distances. The formation of the $[\text{H}_3\text{O}\cdots\text{OH}]^+$ complex is registered when the transferring proton is closer to the acceptor oxygen atom than to the donor oxygen atom, while fragmentation is detected when the distance between H_3O^+ and the OH radical exceeds a predefined limit of 4.5 Å.

SI2. SUPPLEMENTARY TEXT

A. Overview of all detected ions

We recently reported on the detected ion species and their ion yields after the IR-laser-induced strong-field ionization of water dimer in [20]. The new set of measurements at slightly different laser intensities exhibits good agreement of the detected ion species with the previous measurements. In Figure SI4, we provide a graphic overview of all detected ions after IR-strong-ionization of water dimers. Detailed description of the obtained ions, different isotopologues, their ion yields, and expected appearance energies can be found in [20]. Here only briefly - we observe stabilized $(\text{H}_2\text{O})_2^+$, and multiple ion fragments from $(\text{H}_2\text{O})_2^+ / (\text{H}_2\text{O})_2^{2+}$ fragmentation, i. e., H_2O_2^+ , HO_2^+ , O_2^+ , H_3O^+ , H_2O^+ , OH^+ , O^+ , H_3^+ , H_2^+ , H^+ , and their isotopologues.

Each of the ions is represented in Figure SI4 by a projection of the generated Newton sphere after the $(\text{H}_2\text{O})_2^+ / (\text{H}_2\text{O})_2^{2+}$ fragmentation into coordinates of y -position of arrival and time-of-flight recalibrated into the apparent mass-over-charge. A typical example of such a projection is the signal of H_2O^+ with a broad signal blob at the center of ions populated after $(\text{H}_2\text{O})_2^+$ fragmentation and a larger ring feature corresponding to ions populated after the Coulomb explosion of $(\text{H}_2\text{O})_2^{2+}$. At $m/q = 36$ u/e, we observe an intense narrow blob corresponding to the parent ion $(\text{H}_2\text{O})_2^+$ [20].

B. Radial distributions of detected ion channels

Figure SI5 provides an overview of all analyzed ions resulting from $(\text{H}_2\text{O})_2^+$ and $(\text{H}_2\text{O})_2^{2+}$ fragmentation. While the contribution from $(\text{H}_2\text{O})_2^+$ exhibits broad, "blob-like" features from 0 eV to ≈ 1 eV, the contribution from the $(\text{H}_2\text{O})_2^{2+}$ Coulomb explosion displays narrow bands in the H_3O^+ , H_2O^+ , OH^+ , and O^+ radial distributions with high kinetic energy centred around 2 eV due to the repulsion of charged fragments. The green arrows indicate the ranges used to filter ions originating from the $(\text{H}_2\text{O})_2^+$ fragmentation.

In the analysis, we did not use the bottom part of some of the velocity map images due to a strong background signal originating from the diffused water in the spectrometer chamber.

C. Pump-probe signal of detected ion channels

Applying the regions of interest shown in Figure SI5, we selected only ions originating from $(\text{H}_2\text{O})_2^+$ fragmentation and plotted their pump-probe signal dependence in Figure SI6. The signal was corrected for molecular beam intensity as the data acquisition took several days. All channels except for H_3^+ and H_2^+ show strong pump-probe dependence induced by disruptive probing pulse. Notice

that pump-probe signals of $(\text{H}_2\text{O})_2^+$ and H_3O^+ show signal bleaching in $t > 0$ fs. This reflects that the disrupting pulse is causing ion signal migration to other channels.

In this work, we focus on the signal of $(\text{H}_2\text{O})_2^+$, H_3O^+ , H_2O^+ , OH^+ , O^+ , and H^+ . Transient signals of these channels were also analysed by fitting the model based on a set of first-order differential equations with a Gaussian function as a source described in Equation SI1.

The resulting fits are shown as red traces in Figure SI6, and the extracted parameters are summarized in Table SI1. While the $(\text{H}_2\text{O})_2^+$, H^+ , and O^+ traces are well described by a single-term EMG model, the other ion species presented in Figure SI6 require a double-term EMG model.

D. DP signal correlations

The disruptive probing field perturbs the ongoing fragmentation dynamics in $(\text{H}_2\text{O})_2^+$, resulting in a redistribution of the ion signal across different ion channels. This redistribution can be tracked by analyzing correlations among the transient signals of individual ion species. In the most straightforward approach, such correlations can be examined without utilizing the kinetic energy information.

A clear correlation is observed between the transient signals of $(\text{H}_2\text{O})_2^+$ and H^+ , whose summation yields a flat pump-probe trace. This behavior is also reflected in the fitted amplitudes, which exhibit equal magnitudes but opposite signs, and in the characteristic time constants on the order of ~ 1 ps. In a similar fashion, we investigated the correlation between the bleaching of the H_3O^+ transient signal and the rising signals of the H_2O^+ , OH^+ , and O^+ channels. To this end, pairs of H_2O^+ , OH^+ , and O^+ transients were summed with the H_3O^+ signal, and the resulting traces were fitted using the EMG model described in Equation SI1.

The resulting transient signals and their corresponding fits are shown in Figure SI7. The extracted characteristic times are in excellent agreement with the time constants of the omitted ion channel, confirming the underlying correlations. All fitted time constants are summarized in Table SI2.

So far, the kinetics were analyzed for individual ion species across all kinetic energies, and the kinetic energy information obtained from the VMI approach was primarily used to filter out ions originating from Coulomb explosion channels. In this section, we extend the use of kinetic energy information assigned to each detected ion to further decompose the acquired transient signals.

The kinetic energy range for each ion species resulting from $(\text{H}_2\text{O})_2^+$ fragmentation was divided using non-linear binning. We applied the EMG model to fit the transient signals and remove contributions from the cross-correlation and constant background terms. After background subtraction, we performed Pearson correlation analysis on the cleaned transient signals. The results of this analysis are presented in Figure SI8 for H_3O^+ with

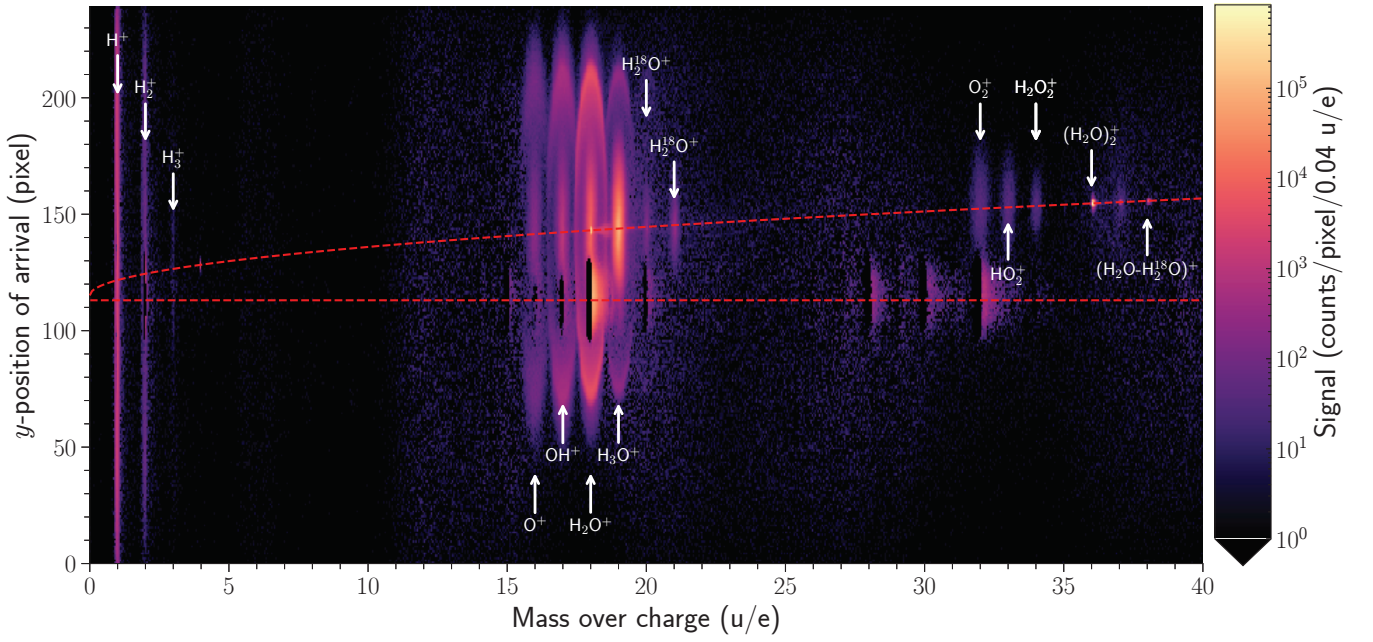


FIG. SI4. Map of the ion signal according to the mass-over-charge ratio and the position of arrival on the detector. The curved dashed line intersects the individual VMI image centers, shifted due to the molecular beam velocity.

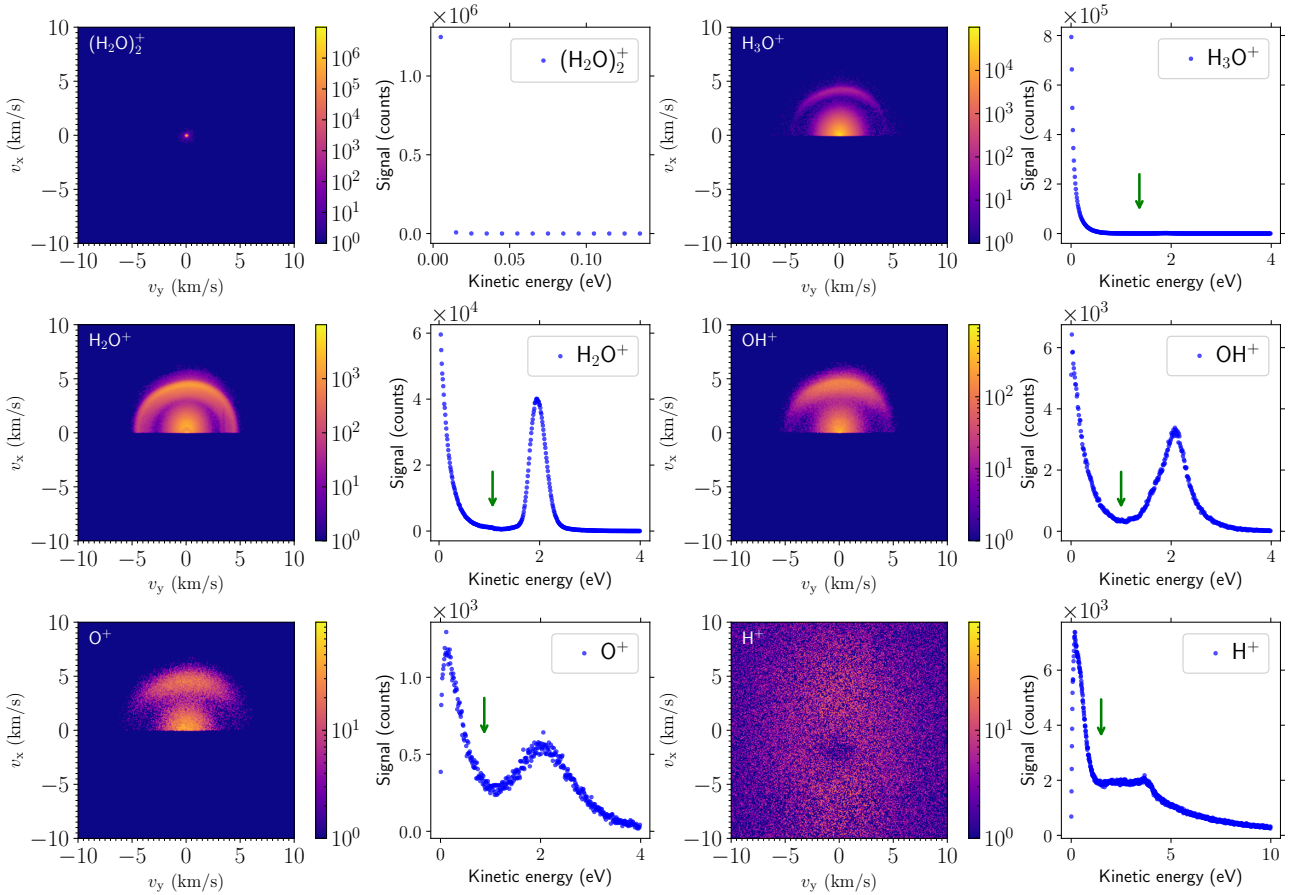


FIG. SI5. Overview of ion velocity map images originating from $(\text{H}_2\text{O})_2^+$ and $(\text{H}_2\text{O})_2^{2+}$ fragmentation and corresponding kinetic energy distributions (KEDs). The KEDs were obtained using 3D momentum calibration. The green arrows show the ranges applied for the selection of the slow ions originating from $(\text{H}_2\text{O})_2^+$ fragmentation.

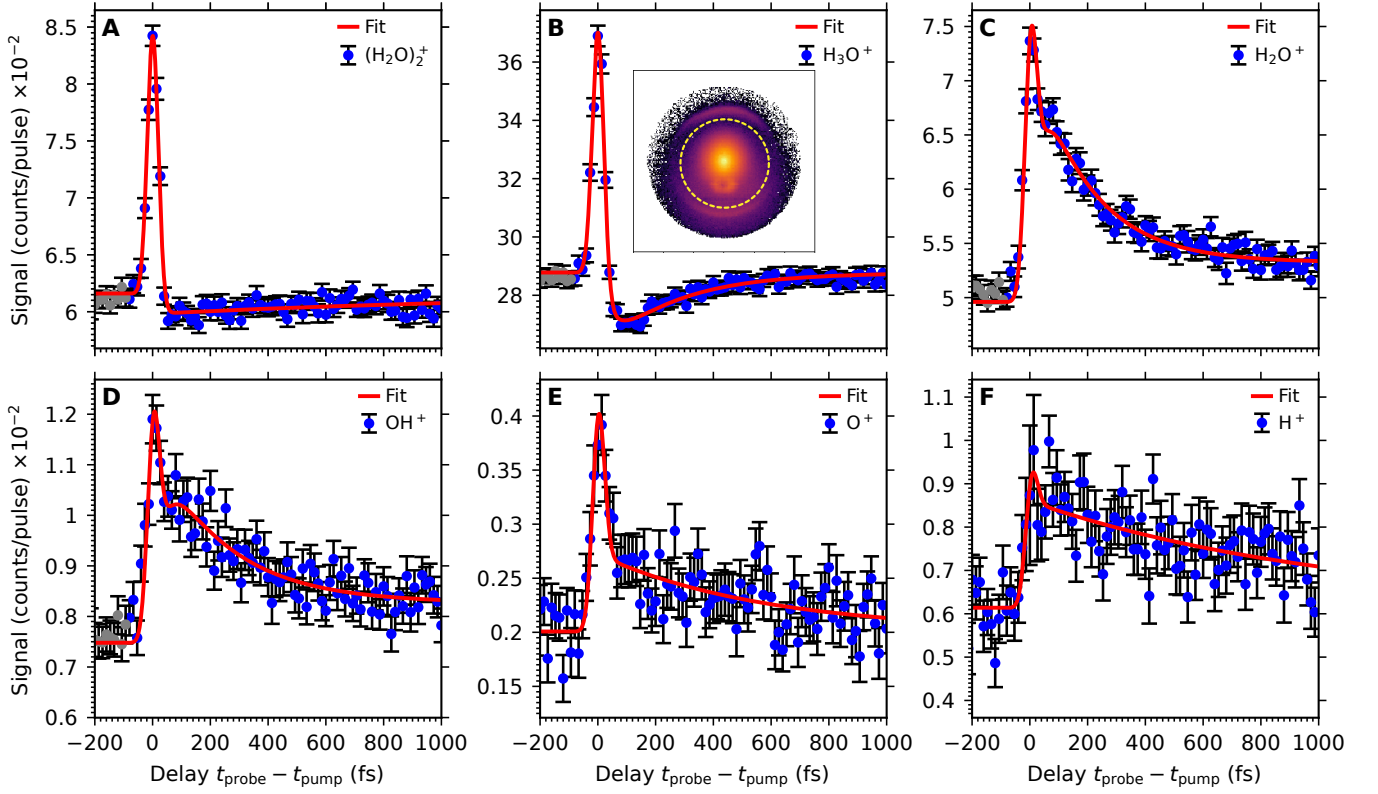


FIG. SI6. Transient signals of the fit of the most prominent ion channels. Panels A–F display $(\text{H}_2\text{O})_2^+$, H_3O^+ , H_2O^+ , OH^+ , O^+ , and H^+ , respectively; see Section SI2 A for details on detected species and channel selection. Red traces represent fits using the parametric model based on exponentially-modified-Gaussian (EMG) functions described in Section SI1. The gray data points in the range $(-500, -50)$ fs were excluded from the fitting procedure due to probe-induced pre-excitation effects. The inset in panel B shows a velocity map of H_3O^+ , whose central part, originating from $(\text{H}_2\text{O})_2^+$ dynamics, is marked with a yellow-dashed circle.

TABLE SI1. Summary of all obtained parameters from the characterization of the pump–probe signals presented in Figure SI6 using the EMG model described in Section SI1.

$[\text{Ch}^+]$	a_{IRF}	$2.35 \cdot \sigma_{\text{IRF}}$	a_1	τ_1	a_2	τ_2	a_θ	$[\text{Ch}^+]_0$
X^+	$[\text{X}^+]/\text{pulse}$	fs	$[\text{X}^+]/\text{pulse}$	fs	$[\text{X}^+]/\text{pulse}$	fs	$[\text{X}^+]/\text{pulse}$	$[\text{X}^+]/\text{pulse}$
$(\text{H}_2\text{O})_2^+$	1.13(3)	44.9(14)	-2.33(65)	1307(445)	-	-	-	0.0616(1)
H_3O^+	4.28(11)	46.8(11)	-6.97(39)	250(28)	1.09(38)	39(9)	-	0.2877(2)
H_2O^+	1.01(6)	48.6(0)	3.88(22)	199(24)	-0.51(17)	26(6)	0.00366(32)	0.0496(2)
OH^+	0.19(2)	48.6(44)	0.78(12)	249(75)	-0.10(7)	33(15)	0.00076(17)	0.0075(1)
O^+	0.09(1)	48.6(16)	0.41(6)	578(119)	-	-	-	0.0020(0)
H^+	0.08(2)	47.0(94)	2.60(38)	1056(194)	-	-	-	0.0061(1)

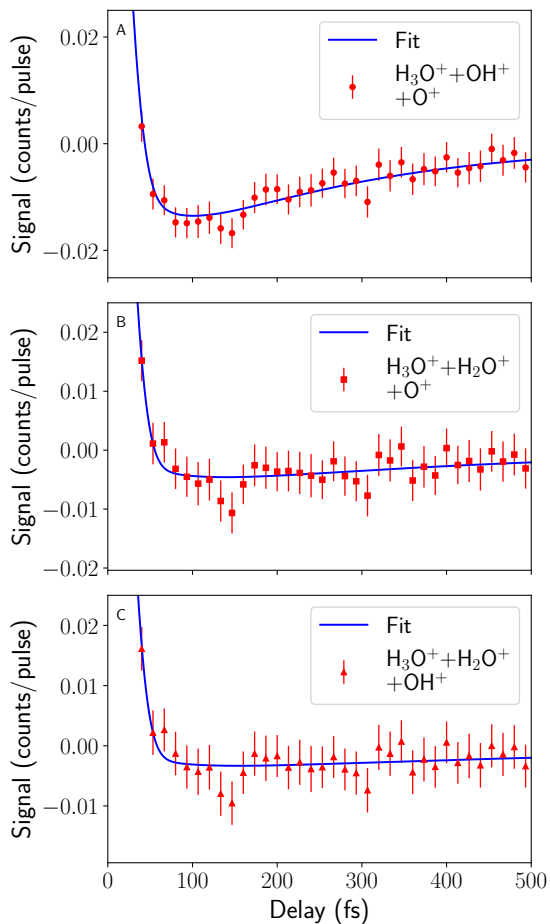


FIG. SI7. Summed transient signals of various ion channels with the fitted parametric model described by Equation S11.

other species.

Figure SI8 reveals the redistribution of ion signal from the H_3O^+ channel to the H_2O^+ , OH^+ , and O^+ channels. Strong anti-correlation (blue regions) indicates signal depletion in H_3O^+ accompanied by signal increase in the correlated ion channels, representing transitions due to disruptive probing. Conversely, positive correlation (red regions) suggests that multiple ion species may originate from a shared parent pathway and exhibit similar dynamic behavior.

Specifically, H_3O^+ ions with kinetic energy below 0.15 eV correlates negatively with the population of H_2O^+ ions in the (0.05, 0.6) eV range, and shows weaker anti-

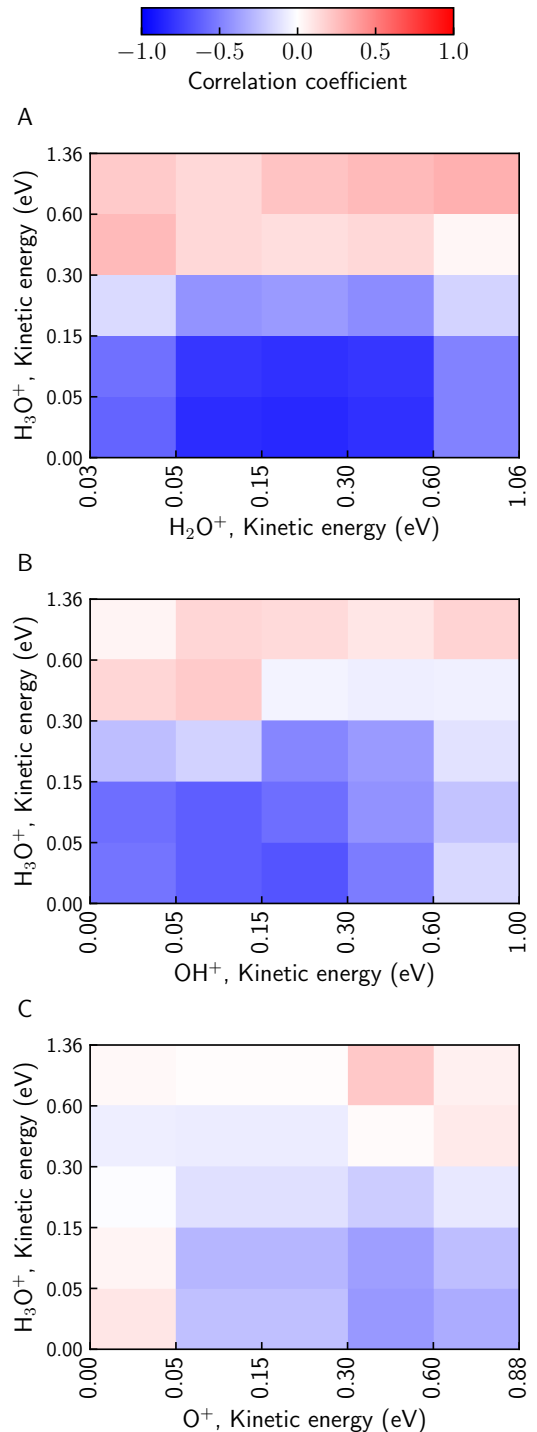


FIG. SI8. Energy-resolved correlation matrices of H_3O^+ with (A) H_2O^+ , (B) OH^+ , and (C) O^+ .

TABLE SI2. Comparison of the fitted lifetimes of summed transient signals of various ion channels and the correlated ion channels.

Summed channels	τ_1 (fs)	Channel	τ_1 (fs)
$\text{H}_3\text{O}^+ + \text{H}_2\text{O}^+ + \text{OH}^+$	550(264)	O^+	578(119)
$\text{H}_3\text{O}^+ + \text{H}_2\text{O}^+ + \text{O}^+$	365(131)	OH^+	386(101)
$\text{H}_3\text{O}^+ + \text{OH}^+ + \text{O}^+$	229(32)	H_2O^+	199(24)

correlation with OH^+ ions up to 0.3 eV and O^+ ions between (0.3, 0.6) eV. For H_3O^+ ions in the (0.15, 0.3) eV range, similar levels of anti-correlation appear with H_2O^+ (0.05, 0.6) eV and OH^+ (0.15, 0.6) eV, along with a minor contribution from O^+ (0.3, 0.6) eV. Finally, H_3O^+ ions with kinetic energies between (0.3, 0.6) eV that are

bleached by the disruptive pulse are redistributed into OH^+ ions in the (0.15, 1) eV range and O^+ ions in the (0, 0.3) eV range. These energy-resolved correlations of various species with H_3O^+ transient signal highlight the various impacts of the disruptive field on the ongoing fragmentation dynamics.

E. Pump-probe dependence of ions' kinetic energy distributions

The ion maps shown in Figure SI9 illustrate the pump-probe dependence of the ion signal as a function of kinetic energy. The first column corresponds to the absolute signal, the second column shows relative changes, and the last column shows relative changes normalized in each row.

F. Kinetic-energy-resolved signal

Figure 2 in the main text shows results of analysis of kinetic-energy-resolved H_3O^+ transient signal. A two-dimensional ion-signal histogram of H_3O^+ with a sudden signal enhancement at time zero in red, corresponding to the cross-correlation peak, and the signal depletion at positive delays in blue is displayed in Figure SI9 B. Analogous to the individual-ion-channel analysis, we applied the parametric EMG model across ten predefined kinetic-energy ranges up to 1.36 eV; this upper limit was chosen to avoid overlap with the Coulomb-explosion channel, as illustrated in Figure SI5 and in the inset of Figure SI6 A. We observed distinct time-dependences among the individual datasets corresponding to the specific kinetic-energy release. All fits are shown in Figure SI10. For instance, the top dataset obtained from H_3O^+ ions with KE in the range of (0.0, 0.05) eV shows signal bleach following the cross-correlation signal in contrast with the bottom dataset obtained for H_3O^+ ions with KE in the range of (0.4, 0.6) eV. See also the main text for a detailed discussion about the energy-resolved observations made from H_3O^+ data.

Similar to the H_3O^+ case, we obtain an energy-resolved map of the H^+ transient signal after subtracting pump-only contributions shown in Figure 3 in the main text. Most of the redistributed $(\text{H}_2\text{O})_2^+$ signal appears in H^+ ions with kinetic energies between 0.3 and 1.5 eV, with lifetimes of 0.7–1.4 ps. In contrast, we observe a rapid bleach within the first 100 fs at kinetic energies below 0.1 eV, which cannot be attributed to a depletion of cross-correlation. Notably, in the 0.1–0.3 eV range, the transient H^+ signal exhibits an oscillatory modulation with a period of approximately 250 fs, as illustrated in Figure SI11. The origin of the oscillations remains unresolved.

TABLE SI3. Characteristic $1/e$ -timescales τ_{PT} and $\tau_{\text{H}_3\text{O}^+}$ from trajectory simulations, describing $[\text{H}_3\text{O} \cdots \text{OH}]^+$ formation via proton transfer and subsequent fragmentation into H_3O^+ across different electronic states. The applied parametric model is discussed in Section SI1 B 1.

State	D ₀	D ₁	D ₂	D ₃
τ_{PT} (fs)	38(1)	85(2)	71(2)	81(4)
$\tau_{\text{H}_3\text{O}^+}$ (fs)	259(19)	413(10)	725(31)	212(6)

G. *Ab initio* electronic-state resolved trajectory simulations

The interpretation of the experimental data is facilitated by *ab initio* calculations. As in earlier studies [21, 22], we populated $(\text{H}_2\text{O})_2^+$ in experiment via strong-field ionization, raising the question of which electronic states drive its dynamics. Our recent study [23] showed that ionization predominantly accesses the four energetically lowest states, D₀–D₃, which *ab initio* simulations [10] found to undergo proton transfer on distinct sub-100 fs timescales. Across all four considered electronic states, the primary dynamical process is ultrafast proton transfer, forming the ion–radical complex $[\text{H}_3\text{O} \cdots \text{OH}]^+$. This complex either stabilizes, a channel observed dominantly in the D₀ state, or fragments to yield a separated H_3O^+ ion and OH radical. Here, we extend the simulations to 1 ps, allowing us to resolve fragmentation pathways beyond the initial PT event.

Figure SI12 provides simulated time-dependent relative branching into the most dominant channels initialized at the four electronic states, D₀–D₃. Our simulations show that a portion of $[\text{H}_3\text{O} \cdots \text{OH}]^+$ complexes remain intact to 1 ps. A smaller fraction of trajectories, indicated by blue lines, on the D₀–D₂ states yield a weakly bound $[\text{H}_2\text{O} \cdots \text{H}_2\text{O}]^+$ complex with hemi-bonded structure [24–26]. Here, the values converged to non-zero channel ratios at 1 ps. In addition, the D₂ and D₃ states display enhanced fragmentation into $\text{H}_2\text{O}^+ + \text{H}_2\text{O}$, indicated by orange lines, compared to the other states. Furthermore, less common fragmentation pathways – including OH^+ formation, proton ejection, and stabilization of more complex ionic species such as H_2O_2^+ – become increasingly prominent with increasing ionization energy, rising from below 2% at D₀ to about 20% in D₃ at the time of 1 ps. Single-exponential fits to the $[\text{H}_3\text{O} \cdots \text{OH}]^+$ formation and H_3O^+ fragmentation channels yield lifetimes of the proton migration τ_{PT} and fragmentation $\tau_{\text{H}_3\text{O}^+}$, see Table SI3, which characterize the averaged early-phase post-ionization dynamics of individual electronic states.

H. Fitting of pump–probe ion signal

The applied model described by Equation SI1 is result of the convolution of IRF function with a delta function δ representing the initial source and cross-correlation signal,

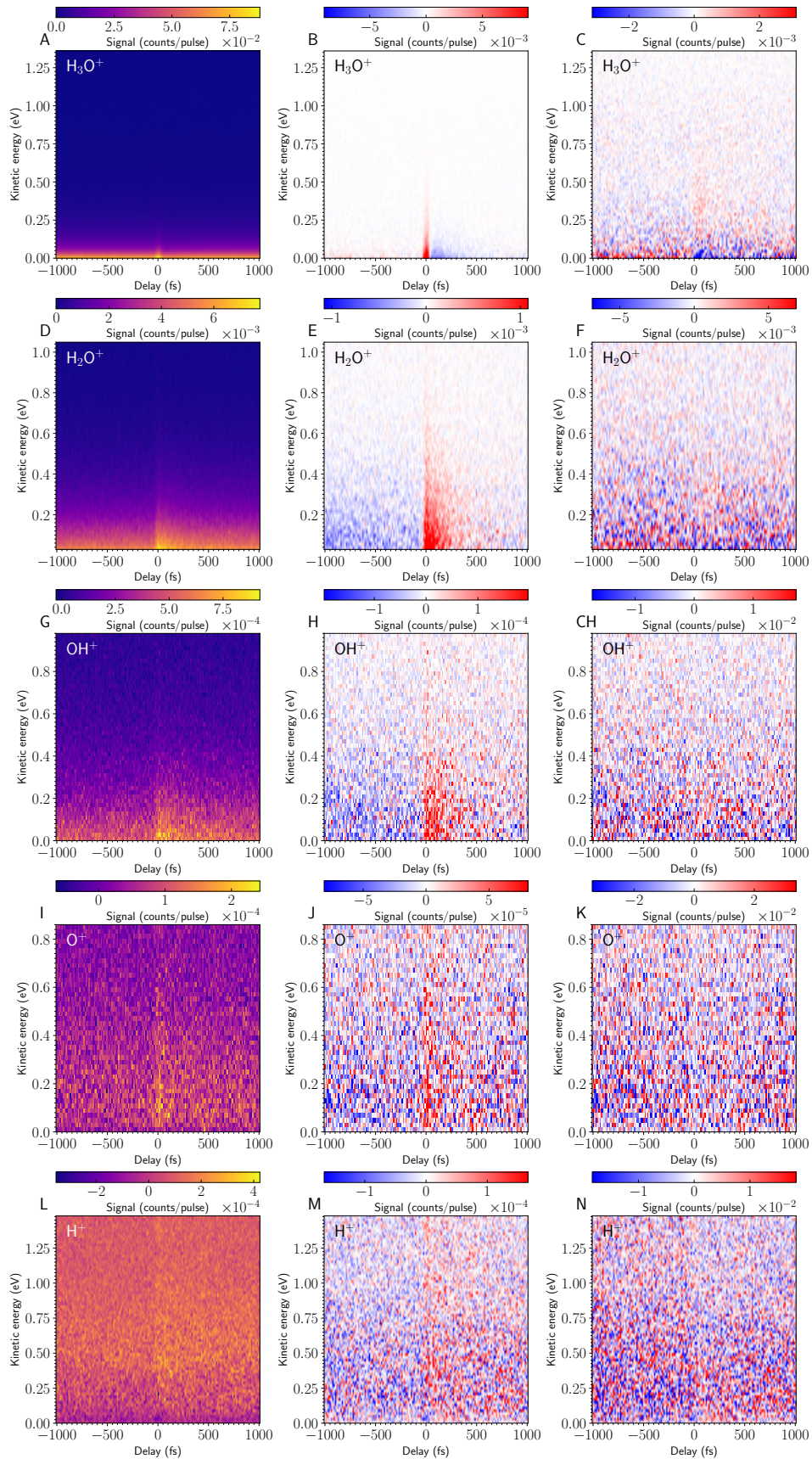


FIG. S19. Ion maps representing the energy-resolved pump-probe dependence of the individual ion channels. The first column corresponds to the absolute signal, the second column shows relative changes from pump-only signal level, and the last column shows relative changes normalized in each row.

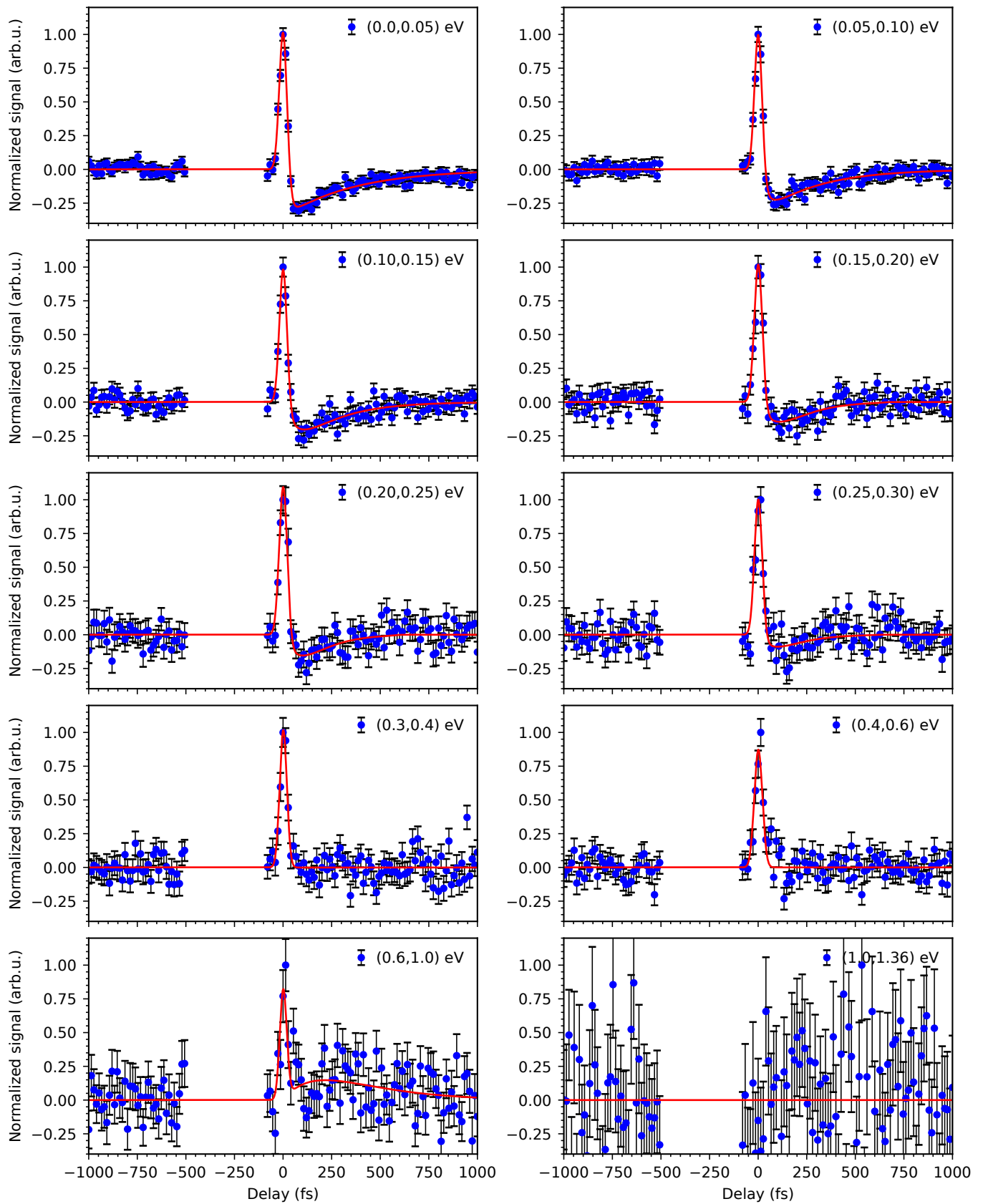


FIG. S110. Transient signals of H_3O^+ at selected kinetic energy ranges. The data were fitted using the parametric EMG model described in Section S11.

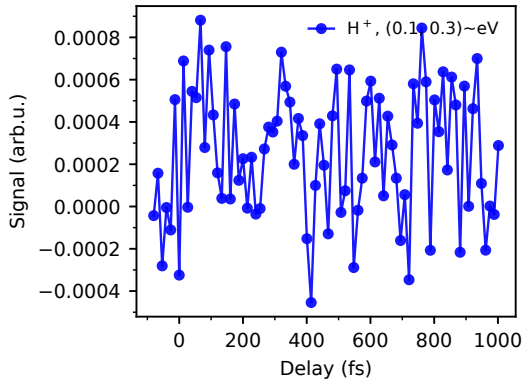


FIG. SI11. Oscillatory component of the H^+ ion signal in the kinetic energy range of 0.1–0.3 eV.

summation over various exponential functions reflecting the investigated dynamics, and heavy-side function corresponding to the secondary fragmentation of previously

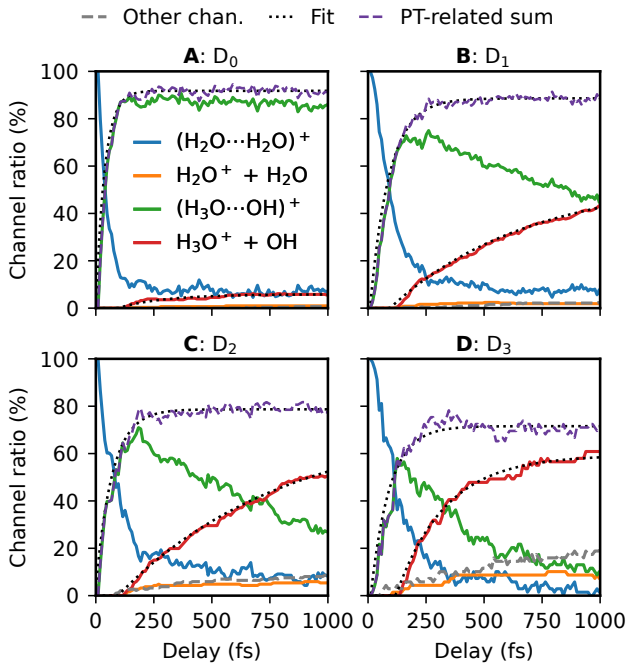


FIG. SI12. *Ab initio* trajectory simulations of $(\text{H}_2\text{O})_2$ dynamics after single ionization into the four lowest electronic states (D_0 – D_3). The curves show the time-dependent relative populations of the main ion–radical channels: $[\text{H}_2\text{O}\cdots\text{H}_2\text{O}]^+$ (blue), $\text{H}_2\text{O}^+ + \text{H}_2\text{O}$ (orange), $[\text{H}_3\text{O}\cdots\text{OH}]^+$ (green), and $\text{H}_3\text{O}^+ + \text{OH}$ (red), with the cumulative contribution of the remaining minor channels shown as a gray dashed line. Channels attributed to proton transfer (dashed violet) and fragmentation into $\text{H}_3\text{O}^+ + \text{OH}$ were fitted with single-exponential models (black dotted).

stabilized ion fragments

$$[\text{Ch}^+] (t; a_{\text{IRF}}, \sigma_{\text{IRF}}, \{a_k\}, \{\tau_k\}, a_\theta) = g(t; a_{\text{IRF}}, \sigma_{\text{IRF}}) * \left(\delta(t) + \sum_k \exp_k(t; a_k, \tau_k) + \Theta(t; a_\theta) \right), \quad (\text{SI5})$$

where we omitted the constant term $[\text{Ch}^+]_0$, which is not connected to the searched dynamics. Equation SI5 reflects that our model in the main text is based on first-order linear differential equations with a Gaussian function as a source.

In the main text, we apply an additional constraint on the amplitudes of EMG and rate constants for observed dynamics with double EMG shape

$$a_1 \cdot k_1 = -a_2 \cdot k_2. \quad (\text{SI6})$$

We derived this condition based on the assumption that the final ion product is populated from a metastable state. The differential equations describing such a scenario are

$$\frac{d[1]}{dt} = g(t) - k_{1 \rightarrow 2}[1] - k_{1 \rightarrow 4}[1], \quad (\text{SI7})$$

$$\frac{d[2]}{dt} = +k_{1 \rightarrow 2}[1] - k_{2 \rightarrow 3}[2], \quad (\text{SI8})$$

$$\frac{d[3]}{dt} = +k_{2 \rightarrow 3}[2], \quad (\text{SI9})$$

where we marked the population of states as $[x]$, $x \in \{1, 2, 3\}$ and $k_{x \rightarrow y}$ are the rate constants, i. e., $k_{x \rightarrow y} > 0$. Furthermore, assuming zero population of [1] in negative times, $t < 0$, we obtain a solution for [2] state population equal to

$$[2](t; k_{1 \rightarrow 2}, k_{2 \rightarrow 3}, k_{1 \rightarrow 4}, \sigma) = \frac{k_{1 \rightarrow 2}}{2(k_{1 \rightarrow 2} + k_{1 \rightarrow 4} - k_{2 \rightarrow 3})} \times [g(t; k_{2 \rightarrow 3}, \sigma) - g(t; k_{1 \rightarrow 2} + k_{1 \rightarrow 4}, \sigma)], \quad (\text{SI10})$$

where the decay function $g_k(t; \sigma)$ is defined as

$$g(t; k, \sigma) = e^{-kt + \frac{1}{2}k^2\sigma^2} \left(1 + \text{Erf} \left(\frac{t - k\sigma^2}{\sqrt{2}\sigma} \right) \right). \quad (\text{SI11})$$

The formula for EMG is equal to

$$\text{EMG}(t; a, k, \sigma) = \frac{a \cdot k}{2} g(t; k, \sigma), \quad (\text{SI12})$$

where a is amplitude of EMG. Through comparison of Equation SI10, Equation SI11, and Equation SI12, we obtain the additional constraint Equation SI6 for fitting dynamics with the double EMG model.

For a comparison of the fitting results presented in Table 1 in the main text using non-varying t_0 and upper

limit $\sigma_{\text{IRF}}^{\text{max}}$, we also show the estimated fitting parameters in case that both the parameters were set free in Table SI4. This illustrates the broad range of obtained values of t_0 and σ_{IRF} , see e. g., H_2O^+ , H_3O^+ , and OH^+ channels for comparison. We assume that the broad widths characterized by σ_{IRF} in the range from 60 fs originate from the underlying fast dynamics. Therefore, in the fitting presented in the main text we applied an upper limit for σ_{IRF} to reveal the fast dynamics occurring on the tenths of femtosecond timescale.

TABLE SI4. Summary of all obtained parameters from the fitting of the pump–probe signal when using the model described by Equation 1 in the main text with varying t_0 and σ_{IRF} parameters.

ion	a_{IRF}	t_0	$2.35 \cdot \sigma_{\text{IRF}}$	a_1	τ_1	a_2	τ_2	a_θ	I_0
X^+	$[X^+]/\text{pulse}$	fs	fs	$[X^+]/\text{pulse}$	fs	$[X^+]/\text{pulse}$	fs	$[X^+]/\text{pulse}$	$[X^+]/\text{pulse}$
$(\text{H}_2\text{O})_2^+$	1.12(3)	2.37(61)	44.4(14)	-2.26(55)	1181(356)	-	-	-	0.0616(1)
H_3O^+	4.34(13)	3.02(57)	47.0(11)	-6.88(36)	268(26)	0.69(28)	27(9)	-	0.2879(2)
H_2O^+	0.86(12)	-5.81(243)	48.8(39)	3.95(21)	205(20)	-0.36(16)	18(7)	0.00376(29)	0.0495(1)
OH^+	0.20(3)	-3.45(404)	64.0(75)	0.78(11)	245(77)	-0.11(9)	35(21)	0.00076(17)	0.0074(1)
O^+	0.10(1)	3.17(312)	62.4(70)	0.42(7)	632(144)	-	-	-	0.0020(0)
H^+	0.10(6)	-2.10(933)	43.5(162)	2.54(36)	986(191)	-0.04(5)	15(20)	-	0.0061(1)

SI3. TUTORIAL ON DISRUPTIVE PROBING

A. Motivation

A recently published paper by Jochim et al. [9] presents a new holistic pump-probe approach called disruptive probing, which can be highly beneficial for the simultaneous tracking of multiple fragmentation pathways after target ionization.

Unfortunately, the description of the time-dependent probing-pulse-induced dynamics, whose effect should reflect the searched original dynamics, was described rather vaguely on the side of the presented description by the kinetics model represented by a set of differential equations.

The following chapters describe seven example situations that illustrate the process of disruptive probing and offer clear insight into the origins of the observed signal dependencies using the differential equation ansatz. This is particularly beneficial for the analysis and subsequent interpretation of the measured data discussed in the main article.

B. Example 1: 3 level model

A model compound ABC, consisting of three distinguishable parts A, B, and C, is ionized into an initial state ABC^{+*} , denoted as i_0 . The compounds of this state can either fragment into $AB^+ + C$ with a rate constant $k_{i_0 \rightarrow AB^+}$ or stabilize as the ABC^+ ion with a rate constant $k_{i_0 \rightarrow ABC^+}$. These processes can be expressed through the following differential equations:

$$\frac{d[i_0]}{dt} = g(t) - k_{i_0 \rightarrow AB^+} [i_0] - k_{i_0 \rightarrow ABC^+} [i_0], \quad (\text{SI13})$$

$$\frac{d[ABC^+]}{dt} = + k_{i_0 \rightarrow ABC^+} [i_0], \quad (\text{SI14})$$

$$\frac{d[AB^+]}{dt} = + k_{i_0 \rightarrow AB^+} [i_0], \quad (\text{SI15})$$

where $g(t)$ is an arbitrary function describing the i_0 population by the ionizing laser pulse. In the paper [9], they apply a Gaussian function $g(t) = \exp\left(-\frac{t^2}{2\sigma_t^2}\right)$ as an approximation of the laser pulse temporal profile, where $\sigma_t = \text{FWHM}_t/2.355$ is the standard deviation. In the simulations below, we also apply a Gaussian function, including the proper normalization factor to ensure the correct units of s^{-1} in

$$g(t) = \frac{1}{\sqrt{2\pi\sigma_t^2}} \exp\left(-\frac{t^2}{2\sigma_t^2}\right) \quad (\text{SI16})$$

The analytic solution of the first differential equation Equation SI13 leads to an exponentially-modified-

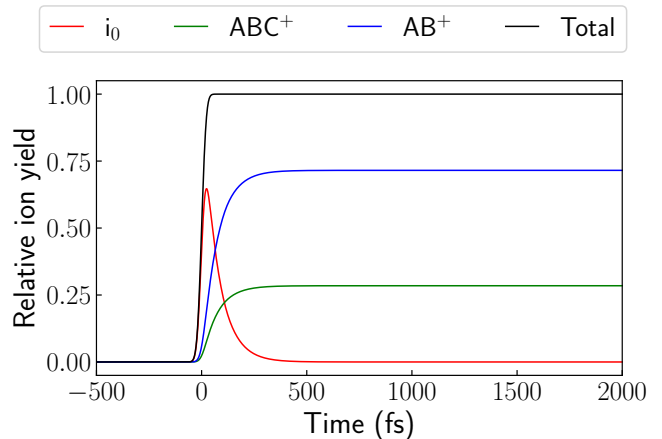


FIG. SI13. Dynamics of the ABC compound after ionization according to Example 1.

Gaussian function

$$[i_0](t, A, \mu, \sigma_t, k_{i_0}) = \frac{Ak_{i_0}}{2} \times \exp\left(k_{i_0} \left(\frac{k_{i_0}\sigma_t^2}{2} - t\right)\right) \times \operatorname{erfc}\left(\frac{k_{i_0}\sigma_t^2 - t}{\sqrt{2}\sigma_t}\right), \quad (\text{SI17})$$

where A is the amplitude and k_{i_0} is the summed rate constant for i_0 decaying into other levels. In the case above, $A = 1$ and $k_{i_0} = k_{i_0 \rightarrow ABC^+} + k_{i_0 \rightarrow AB^+}$.

Alternatively, by numerically solving the set of differential equations SI13–SI15 with the parameters $\sigma_t = (40 \text{ fs})/2.355 = 17 \text{ fs}$, $k_{i_0 \rightarrow AB^+} = 1/(100 \text{ fs})$, and $k_{i_0 \rightarrow ABC^+} = 1/(250 \text{ fs})$, we obtain the signal dependencies for i_0 , AB^+ , and ABC^+ shown in Figure SI13. The goal of our experiment is to measure these dependencies. Since fragmentation occurs on the subpicosecond timescale, it has practically no effect on the observed time-of-flight mass spectra and velocity map images (mass spectrometric features assigned to metastable ions would exhibit particular features from the nanosecond timescale of fragmentation), we want to apply a disruptive probing technique to obtain them.

1. Simulation of disruptive probing

In disruptive probing, a second weak probing pulse interacts with an ensemble of ionized particles undergoing relaxation processes. The probing pulse should be weak enough to affect the ongoing processes, such as changes in couplings among the states and rate constants through changes in potential energy surfaces, but not change the ion total population. In our simplified

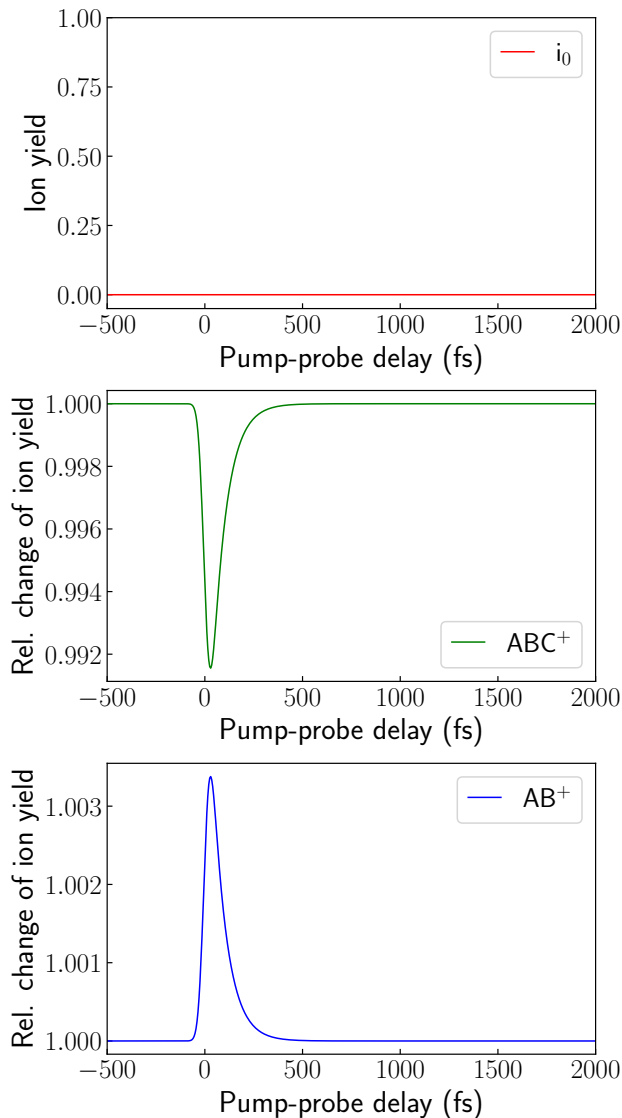


FIG. SI14. Simulated disruptive probing measurement in case of Example 1.

model, the effect of the probing pulse is described by adding new or altered rate constants that represent the weak-probe-pulse-induced couplings. We assume, as in the undisturbed model above, that the rate parameters are constants. To simplify the notation, we incorporate the probe effect on couplings directly into the multiplicative factor of the rate parameters as $(1 + \delta_{X \rightarrow Y} h(t))$, where $\delta_{X \rightarrow Y}$ represents the relative change induced by the probe pulse field and $h(t)$ is a function describing the probing pulse centered at the pump-probe delay τ , i.e., $h(t) = \frac{1}{\sqrt{2\pi\sigma_t^2}} \exp\left(-\frac{(t-\tau)^2}{2\sigma_t^2}\right)$. Here, σ_t of the probing pulse is taken to be equal to the standard deviation of the ionizing pulse. This is a reasonable constraint, as in our experiment, the probing pulse is generated by a beam splitter reflecting a fraction of the pumping pulse.

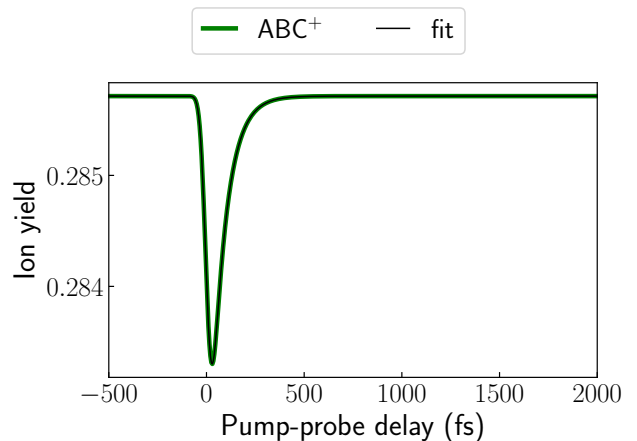


FIG. SI15. Fitted simulated signal dependence of ABC^+ ion from Example 1.

Applying the changes due to the probing pulse, we rewrite Equations SI13–SI15 as follows:

$$\begin{aligned} \frac{d[i_0]}{dt} = & g(t) \\ & - k_{i_0 \rightarrow AB^+} (1 + \delta_{i_0 \rightarrow AB^+} h(t)) [i_0] \\ & - k_{i_0 \rightarrow ABC^+} (1 + \delta_{i_0 \rightarrow ABC^+} h(t)) [i_0] \end{aligned} \quad (\text{SI18})$$

$$\frac{d[ABC^+]}{dt} = + k_{i_0 \rightarrow ABC^+} (1 + \delta_{i_0 \rightarrow ABC^+} h(t)) [i_0], \quad (\text{SI19})$$

$$\frac{d[AB^+]}{dt} = + k_{i_0 \rightarrow AB^+} (1 + \delta_{i_0 \rightarrow AB^+} h(t)) [i_0]. \quad (\text{SI20})$$

The analytic solution of the new set of differential equations is not straightforward, so we will use a numerical solver to simulate the results of the disruptive probing measurement. In the real experiment, we measure the resulting ion yields of different ion fragments at different pump-probe delays. Similarly, by varying the probe delay in the simulation, we can compare the resulting ion populations at a later time, specifically at 3 ps when all fragmentation dynamics are finished, to the ion yields in undisturbed fragmentation (static measurement without the probing pulse). This is shown in Figure SI14.

As expected, i_0 ions show zero population in any pump-probe measurement because the initial population is transferred to ABC^+ and AB^+ ions. The other two ion states exhibit relative signal decreases and increases. This flow of the ion population from one ion fragment type to another is connected to the slight changes in the rate constants, and we would observe similar pump-probe signal dependencies except in cases where $\delta_{i_0 \rightarrow ABC^+} = \delta_{i_0 \rightarrow AB^+}$.

Both ion signal dependencies are equal to the i_0 relative ion yield dependency shown in Figure SI13, multiplied by a constant dependent on the perturbed and unperturbed rate constants. This can be verified by fitting the signal dependencies. Figure SI15 shows the result of fitting the ABC^+ signal. The fitted rate constant is $k^{fit} =$

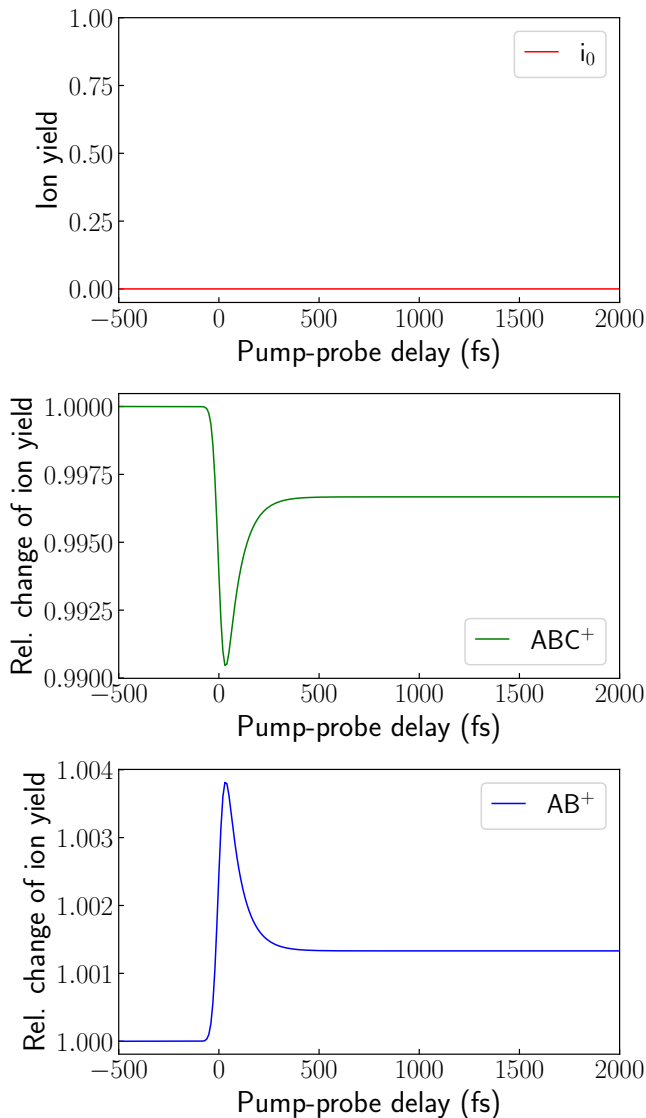


FIG. SI16. Simulated disruptive probing measurement in case of Example 2.

$1/(71.4 \text{ fs})$, which exactly matches $k_{i_0} = k_{i_0 \rightarrow ABC^+} + k_{i_0 \rightarrow AB^+}$. The same rate constant would be obtained from fitting the change in AB^+ ion yield. Thus, from this simple example, we see that qualitative analysis of the disruptive-probing pump-probe signal dependencies provides the rate constant (or lifetime) for the decay of i_0 . To obtain the individual rate constants $k_{i_0 \rightarrow ABC^+}$ and $k_{i_0 \rightarrow AB^+}$, additional information is needed, such as the ratio of ABC^+ and AB^+ ion yields in undisturbed measurements.

Example 1 was the simplest possible model scenario illustrating the disruptive effect in a pump-probe measurement using the disruptive probing technique. The next six examples will introduce additional features that can provide a deeper understanding of the origin of the observed signal dependencies.

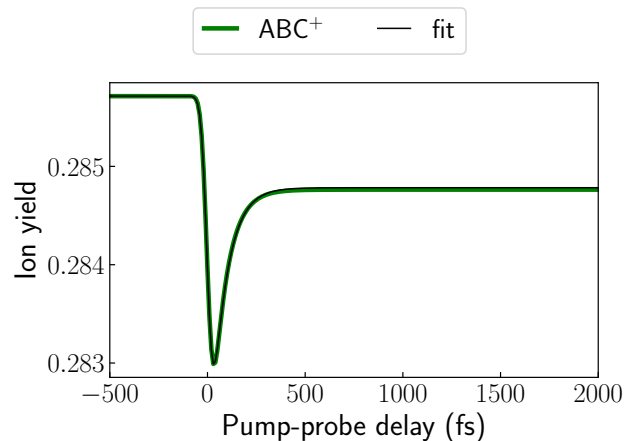


FIG. SI17. Fitted simulated signal dependence of ABC^+ ion from Example 2.

C. Kinetic model: Example 2

Example 2 illustrates a situation similar to that described in Example 1, using the same 3-level system. In this case, the probing pulse induces an additional coupling $k\delta_{ABC^+ \rightarrow AB^+}h(t)$ between ABC^+ and AB^+ ions, resulting in additional fragmentation of ABC^+ . The set of differential equations SI19 and SI20 describing this situation is modified by including an additional term $k\delta_{ABC^+ \rightarrow AB^+} = 1/(300 \text{ fs})$, as follows:

$$\frac{d[ABC^+]}{dt} = +k_{i_0 \rightarrow ABC^+}(1 + \delta_{i_0 \rightarrow ABC^+}h(t))[i_0] - k\delta_{ABC^+ \rightarrow AB^+}h(t)[ABC^+], \quad (\text{SI21})$$

$$\frac{d[AB^+]}{dt} = +k_{i_0 \rightarrow AB^+}(1 + \delta_{i_0 \rightarrow ABC^+}h(t))[i_0] + k\delta_{ABC^+ \rightarrow AB^+}h(t)[ABC^+]. \quad (\text{SI22})$$

The new coupling rate constant is denoted as $k\delta_{X^+ \rightarrow Y^+}$ to indicate that it is induced by the probing laser field represented by $h(t)$. The simulation of the disruptive probing measurement under these conditions is shown in Figure SI16.

A lasting signal step is observed, reflecting that the probing laser-induced couplings transfer part of the ABC^+ population to the AB^+ ion yield. Notice that this transfer is independent of the pump-probe delay due to the additional energy, which destabilizes the ABC^+ ions. The time independence of this feature enables us to distinguish this example from the disruption of an ongoing dynamical process. The question remains if we can retrieve the decay rate of i_0 .

By fitting the pump-probe dependency of ABC^+ with a model function consisting of an exponentially-modified-Gaussian function (Equation SI17) combined with a step function $A \cdot [1 + \text{erf}(\frac{x-\mu}{\sigma})]/2$, we obtain $k^{fit} = 1/(71.1 \text{ fs})$ as an estimate of the i_0 decay rate constant. The fit is

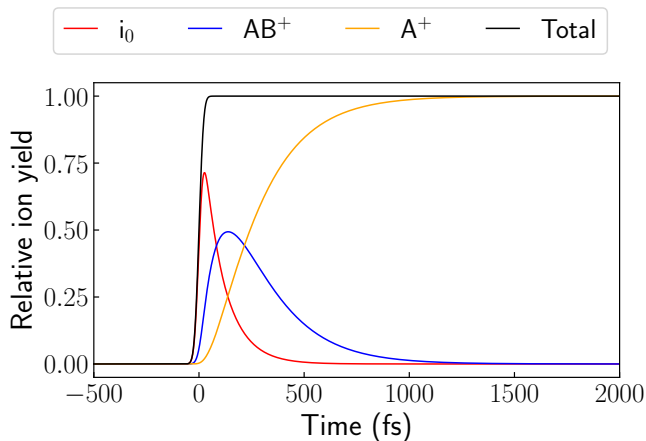


FIG. SI18. Dynamics of the ABC compound after ionization according to the Example 3.

shown in Figure SI17. We would obtain the same result for the dependence of the AB^+ ion signal, but with the opposite sign of the amplitude. The fitted rate constant is slightly (less than 1%) different due to the additional coupling; nevertheless, we still achieve good agreement with the simulated decay rate of i_0 .

Example 2 illustrates that even the additional disruption of the finally detected ions should not prevent the retrieval of the information about the original fragmentation dynamics.

D. Kinetic model: Example 3

The next example of a disruptive probing measurement will be demonstrated using a 3-ionic-state system with sequential decay. The corresponding set of differential equations is written as follows:

$$\frac{d[i_0]}{dt} = g(t) - k_{i_0 \rightarrow AB^+} (1 + \delta_{i_0 \rightarrow AB^+} h(t)) [i_0], \quad (\text{SI23})$$

$$\frac{d[AB^+]}{dt} = + k_{i_0 \rightarrow AB^+} (1 + \delta_{i_0 \rightarrow AB^+} h(t)) [i_0] - k_{AB^+ \rightarrow A^+} (1 + \delta_{AB^+ \rightarrow A^+} h(t)) [AB^+], \quad (\text{SI24})$$

$$\frac{d[A^+]}{dt} = + k_{AB^+ \rightarrow A^+} (1 + \delta_{AB^+ \rightarrow A^+} h(t)) [AB^+], \quad (\text{SI25})$$

where we have included the terms induced by the probing pulse, specifically $\delta_{i_0 \rightarrow AB^+} = 2.5$ and $\delta_{AB^+ \rightarrow A^+} = 4$, as well as the rate constant $k_{AB^+ \rightarrow A^+} = 1/(200 \text{ fs})$. The resulting relative ion signal dependencies of interest are shown in Figure SI18. We can observe that, in the end, the entire population is transferred to the A^+ fragments. Similarly, if the decay-rate-affecting-probing field were

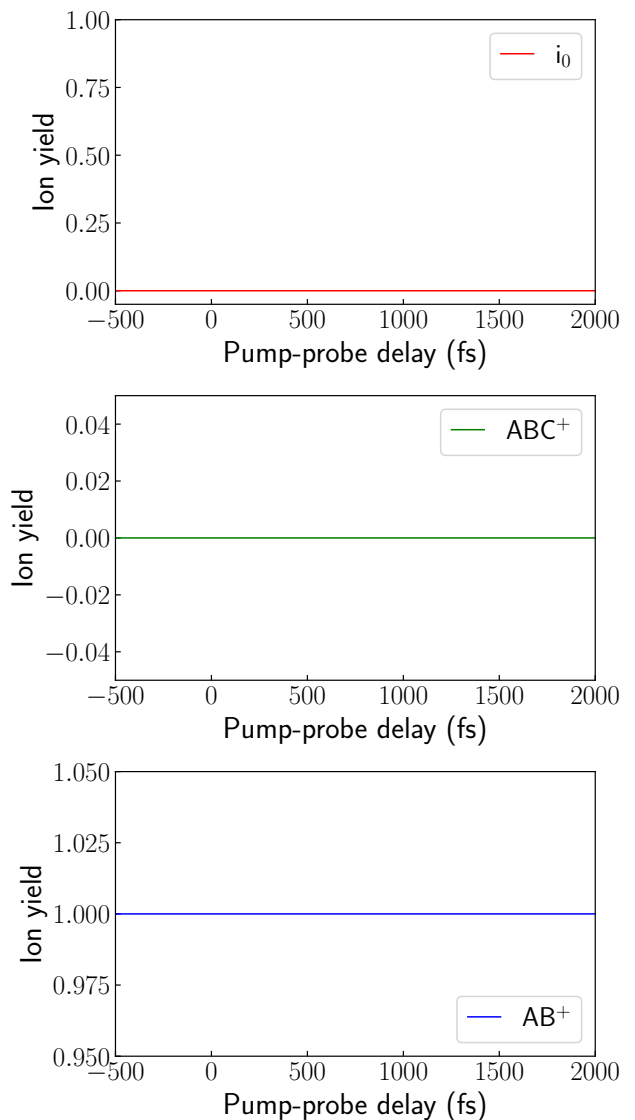


FIG. SI19. Simulated disruptive probing measurement in case of Example 3.

present, all the population would still end up in the A^+ fragments. Therefore, using disruptive probing with the mass spectrometric technique is unable to provide any insight into the ongoing dynamics. This is illustrated in Figure SI19.

E. Kinetic model: Example 4

Similar to Example 3, Example 4 examines the disruptive probing measurement on a system undergoing sequential fragmentation: $i_0 \rightarrow AB^+ \rightarrow A^+$. However, this time there is also an ABC^+ level present. We apply all the constants used in the previous examples, except for the coupling between the ABC^+ and AB^+ levels. The differential equations describing this system, including

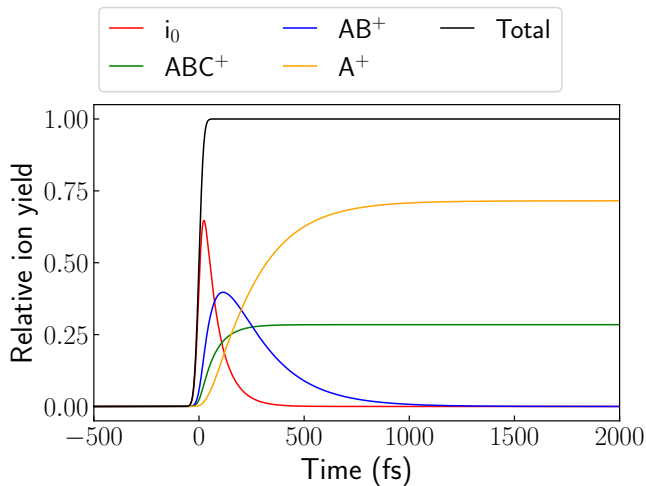


FIG. SI20. Dynamics of the ABC compound after ionization according to the Example 4.

the effects of the probing pulse, are as follows:

$$\frac{d[i_0]}{dt} = g(t) - k_{i_0 \rightarrow AB^+}(1 + \delta_{i_0 \rightarrow AB^+} h(t))[i_0] - k_{i_0 \rightarrow ABC^+}(1 + \delta_{i_0 \rightarrow ABC^+} h(t))[i_0] \quad (\text{SI26})$$

$$\frac{d[ABC^+]}{dt} = +k_{i_0 \rightarrow ABC^+}(1 + \delta_{i_0 \rightarrow ABC^+} h(t))[i_0], \quad (\text{SI27})$$

$$\frac{d[AB^+]}{dt} = +k_{i_0 \rightarrow AB^+}(1 + \delta_{i_0 \rightarrow AB^+} h(t))[i_0] - k_{AB^+ \rightarrow A^+}(1 + \delta_{AB^+ \rightarrow A^+} h(t))[AB^+], \quad (\text{SI28})$$

$$\frac{d[A^+]}{dt} = +k_{AB^+ \rightarrow A^+}(1 + \delta_{AB^+ \rightarrow A^+} h(t))[AB^+]. \quad (\text{SI29})$$

The undisturbed evolution of the states' populations is shown in Figure SI20. This time, the resulting population ends either as A^+ ions from the sequential fragmentation or ABC^+ ions due to i_0 stabilization. Therefore, the disruptive probing measurement will reveal changes in the resulting ion yields, as illustrated in the simulated measurement shown in Figure SI21.

We can see that the outcome of the measurement is the same as in Example 1. For the given values of rate constants, the measurement suggests that the additional level AB^+ is not detected. The fitted rate constant, obtained using an exponentially-modified-Gaussian function, is $k^{fit} = 1/(71.44 \text{ fs})$, which is similar to the decay rate of i_0 .

Example 4 illustrates that in such a case, we are blind to the metastable level, even when an alternative route is present. The next two examples will present opposite situations, where the sequential fragmentation dynamics can be retrieved using the disruptive probing method.

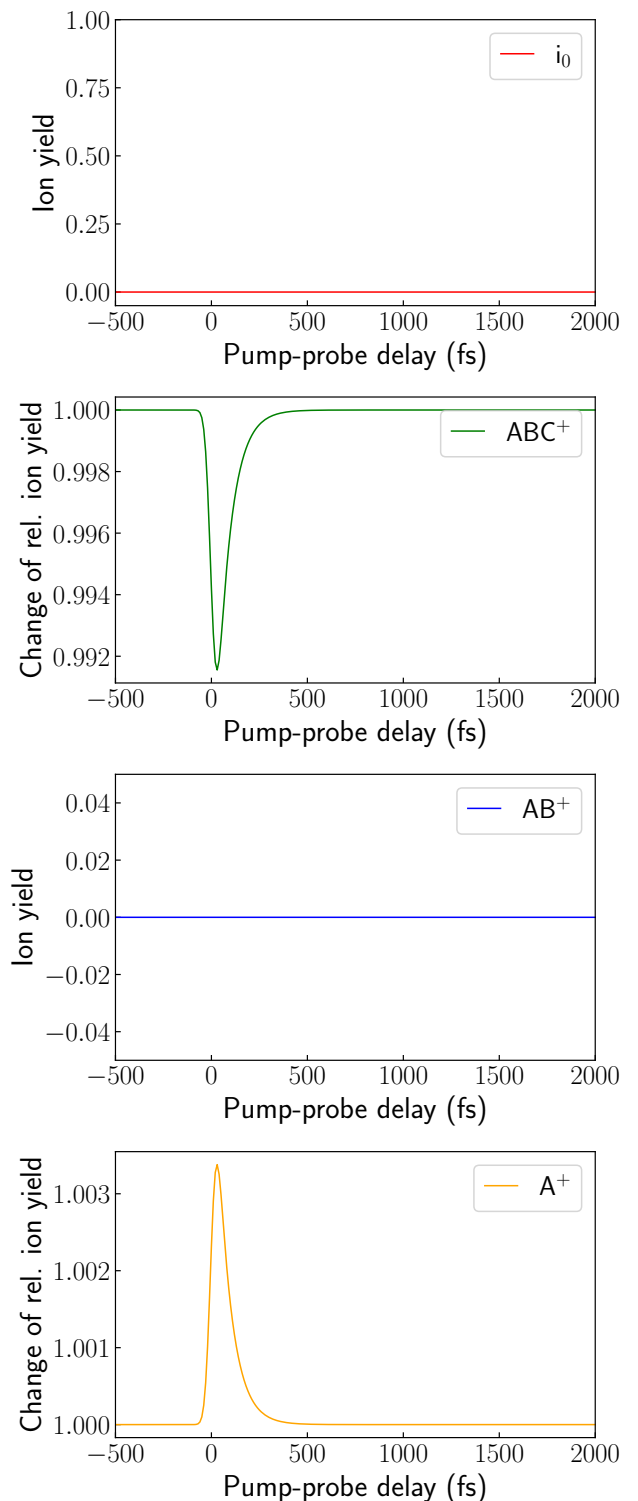


FIG. SI21. Simulated disruptive probing measurement in case of Example 4.

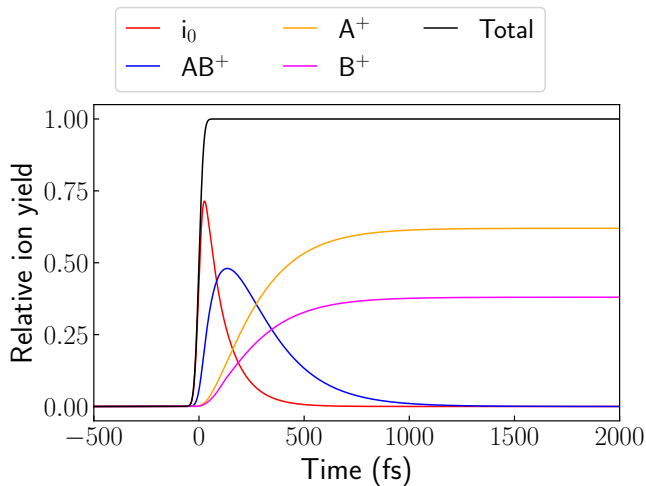


FIG. SI22. Dynamics of the ABC compound after ionization according to the Example 5.

F. Kinetic model: Example 5

The situation changes from the previous example when the two levels result from sequential fragmentation, such as $i_0 \rightarrow AB^+ \rightarrow A^+$ or $i_0 \rightarrow AB^+ \rightarrow B^+$. The new set of differential equations is as follows:

$$\frac{d[i_0]}{dt} = g(t) - k_{i_0 \rightarrow AB^+} (1 + \delta_{i_0 \rightarrow AB^+} h(t)) [i_0] \quad (\text{SI30})$$

$$\begin{aligned} \frac{d[AB^+]}{dt} = & + k_{i_0 \rightarrow AB^+} (1 + \delta_{i_0 \rightarrow AB^+} h(t)) [i_0] \\ & - k_{AB^+ \rightarrow A^+} (1 + \delta_{AB^+ \rightarrow A^+} h(t)) [AB^+] \\ & - k_{AB^+ \rightarrow B^+} (1 + \delta_{AB^+ \rightarrow B^+} h(t)) [AB^+], \end{aligned} \quad (\text{SI31})$$

$$\frac{d[A^+]}{dt} = + k_{AB^+ \rightarrow A^+} (1 + \delta_{AB^+ \rightarrow A^+} h(t)) [AB^+]. \quad (\text{SI32})$$

$$\frac{d[B^+]}{dt} = + k_{AB^+ \rightarrow B^+} (1 + \delta_{AB^+ \rightarrow B^+} h(t)) [AB^+], \quad (\text{SI33})$$

where we set the rate constants as $k_{i_0 \rightarrow AB^+} = 1/(100 \text{ fs})$, $k_{AB^+ \rightarrow A^+} = 1/(300 \text{ fs})$, and $k_{AB^+ \rightarrow B^+} = 1/(500 \text{ fs})$. Additionally, the induced disruption by the probing pulse were set as $\delta_{i_0 \rightarrow AB^+} = 2.5$, $\delta_{AB^+ \rightarrow A^+} = 1$, and $\delta_{AB^+ \rightarrow B^+} = 10$.

By numerically solving the differential equations, one can obtain the ion signal dependencies for the undisturbed case, as shown in Figure SI22, and the simulated result of the pump-probe disruptive probing measurement, illustrated in Figure SI23. The rate fitting using two exponentially modified Gaussian functions, as shown in Figure SI24, reveals the rate constants for the population and decay of the AB^+ ion level. We obtain $k_1^{fit} = 1/(100 \text{ fs})$

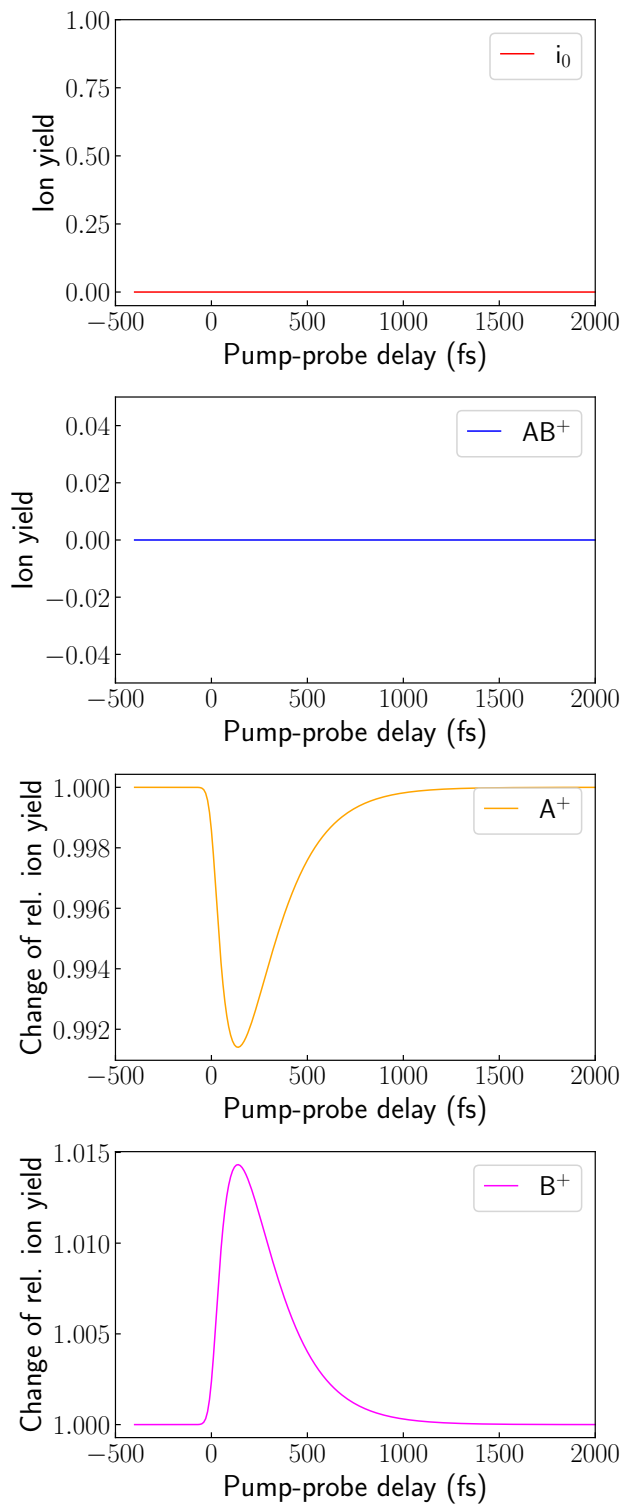


FIG. SI23. Simulated disruptive probing measurement in case of Example 5.

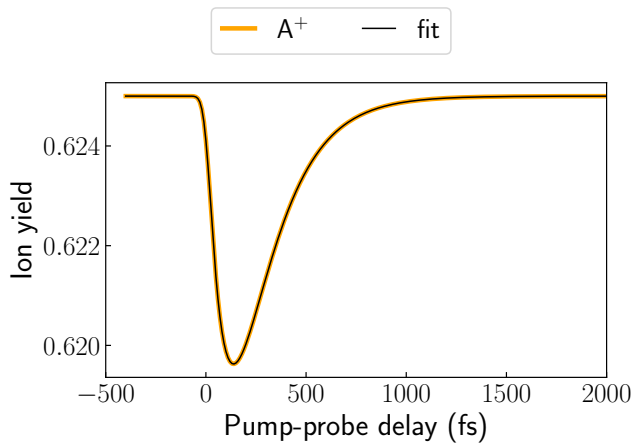


FIG. SI24. Fitted simulated measurement of A^+ ion from Example 5.

and $k_2^{fit} = 1/(187 \text{ fs})$, which correspond to $k_{i_0 \rightarrow AB^+}$ and $k_{AB^+ \rightarrow A^+} + k_{AB^+ \rightarrow B^+}$, respectively.

The sequential pathway splitting into final fragments A^+ and B^+ enables us to detect the rate constant for population and following fragmentation of the metastable AB^+ ion. This is very similar to Example 1, where the population rate was given by a laser pulse time-dependence.

G. Kinetic model: Example 6

The most complex example incorporates all the previous cases, with the addition of the stabilized ABC^+ as an alternative pathway for the populated i_0 state. The dynamics of the five ionic levels, denoted as i_0 , ABC^+ ,

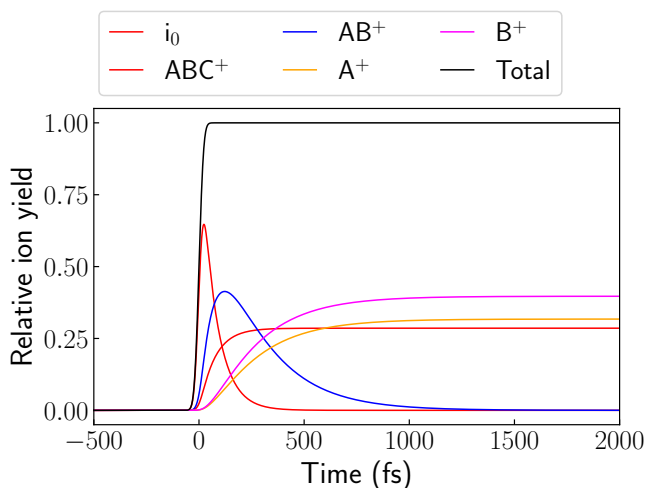


FIG. SI25. Dynamics of the ABC compound after ionization according to the Example 6.

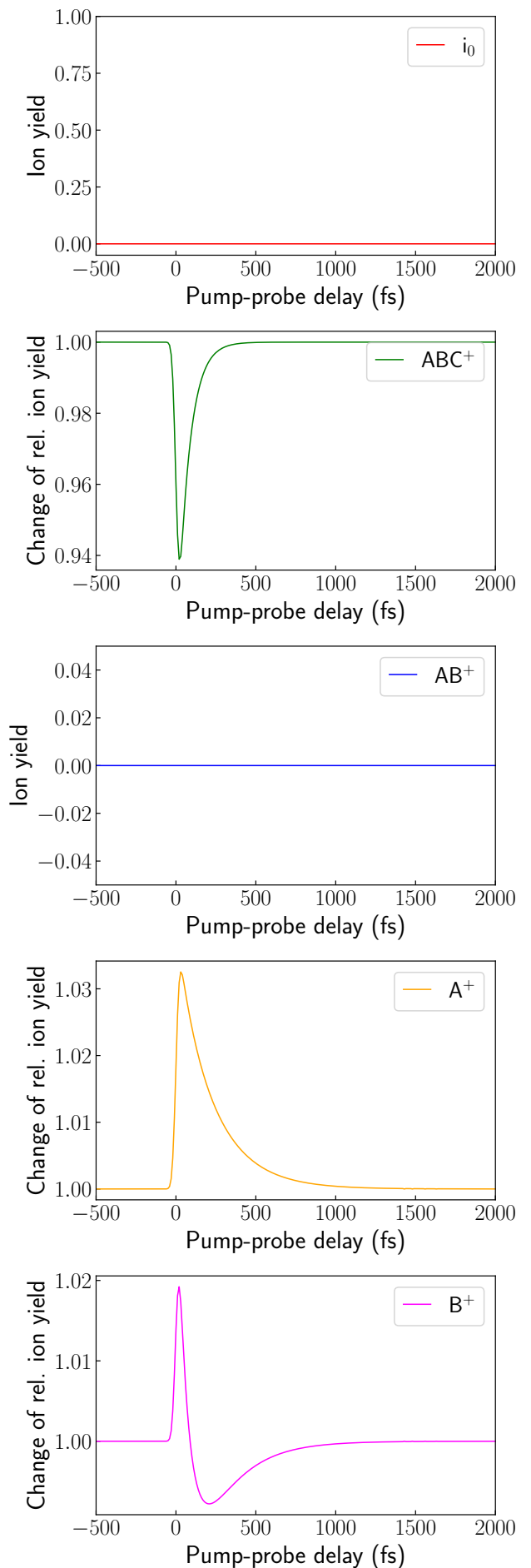


FIG. SI26. Simulated disruptive probing measurement in case of Example 6.

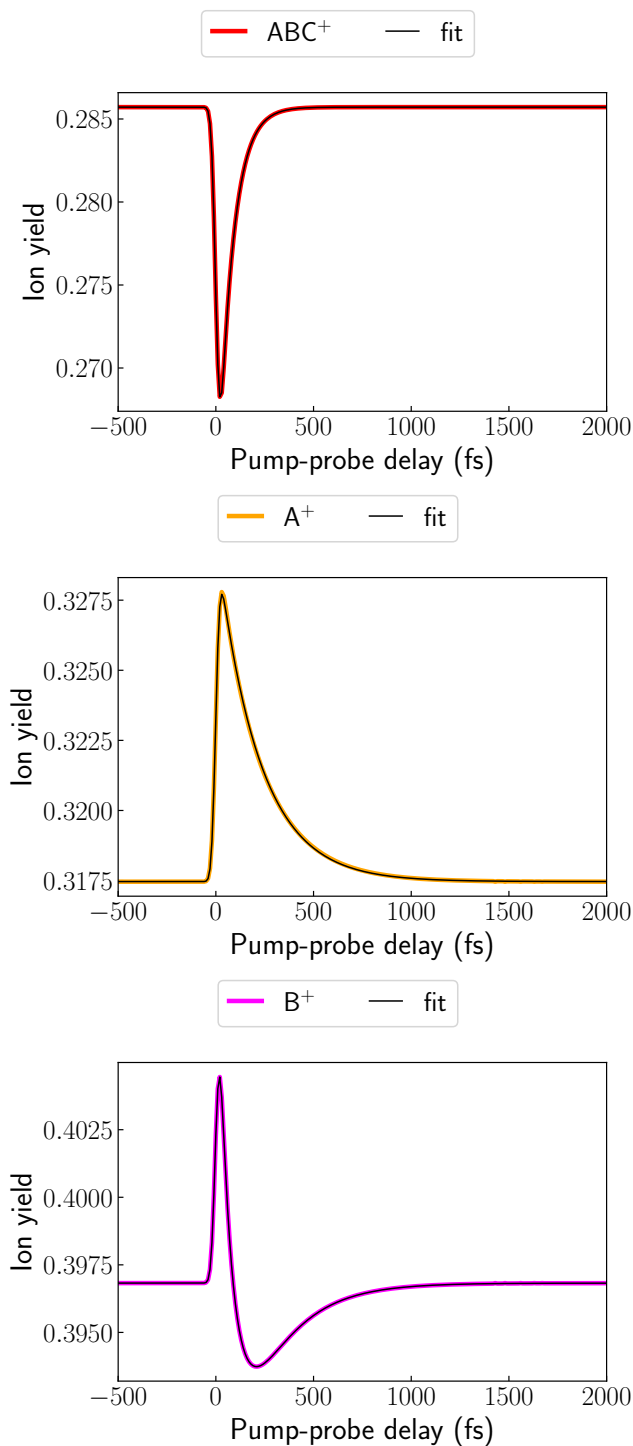


FIG. SI27. Fitted simulated signal dependences of ABC^+ , A^+ , and B^+ ion from Example 6.

AB^+ , A^+ , and B^+ , is described by the following variables:

$$\frac{d[i_0]}{dt} = g(t) - k_{i_0 \rightarrow AB^+}(1 + \delta_{i_0 \rightarrow AB^+} h(t))[i_0] - k_{i_0 \rightarrow ABC^+}[i_0] \quad (\text{SI34})$$

$$\frac{d[ABC^+]}{dt} = +k_{i_0 \rightarrow ABC^+}[i_0], \quad (\text{SI35})$$

$$\frac{d[AB^+]}{dt} = +k_{i_0 \rightarrow AB^+}(1 + \delta_{i_0 \rightarrow AB^+} h(t))[i_0] - k_{AB^+ \rightarrow A^+}(1 + \delta_{AB^+ \rightarrow A^+} h(t))[AB^+] - k_{AB^+ \rightarrow B^+}[AB^+], \quad (\text{SI36})$$

$$\frac{d[A^+]}{dt} = +k_{AB^+ \rightarrow A^+}(1 + \delta_{AB^+ \rightarrow A^+} h(t))[AB^+]. \quad (\text{SI37})$$

$$\frac{d[B^+]}{dt} = +k_{AB^+ \rightarrow B^+}[AB^+], \quad (\text{SI38})$$

where original rate constants are $1/k_{i_0 \rightarrow ABC^+} = 250$ fs, $1/k_{i_0 \rightarrow AB^+} = 100$ fs, $1/k_{AB^+ \rightarrow A^+} = 500$ fs, $1/k_{AB^+ \rightarrow B^+} = 400$ fs, and induced disruptive changes are $\delta_{i_0 \rightarrow AB^+} = \delta_{AB^+ \rightarrow A^+} = 10$. The resulting undisturbed dynamics are shown in Figure SI25. Clearly, the population of each level develops differently.

The simulated measurement result is shown in Figure SI26. All four detected ions, i.e., ABC^+ , AB^+ , A^+ , and B^+ , exhibit different signal dependence in the simulated disruptive probing measurement. Specifically, the ABC^+ ion signal reveals a narrow negative exponentially-modified-Gaussian dependence, similar to the dynamics of the i_0 signal, while the A^+ and B^+ ion signal dependences are linked to the population and decay of the AB^+ ions.

This enables us to obtain three different rate constants just from the data fitting, as shown in Figure SI27. The ABC^+ signal was fitted with a single exponentially-modified-Gaussian function, while the A^+ and B^+ signals were fitted with two exponentially-modified-Gaussian functions. The resulting fits are shown in Figure SI27. The obtained rates of $1/k_{ABC^+}^{\text{fit}} = 71.4$ fs, $1/k_{1A^+}^{\text{fit}} = 71.4$ fs, and $1/k_{2A^+}^{\text{fit}} = 222.2$ fs are in perfect agreement with the used rate constants for the dynamics simulation.

H. Kinetic model: Example 7

The final example shows a different scenario of the disruptive effect. Instead of reshuffling the ions' final population among the existing pathways, like in Examples 1 and 6, or reshuffling the ion signal among the final ion species, like in Example 2, the disrupting pulse opens of a new fragmentation pathway leading to detection of a new ion species. This can be described in differential

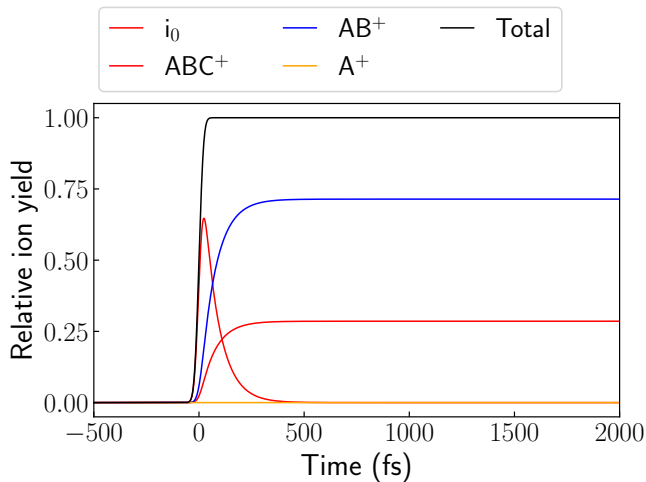


FIG. SI28. Dynamics of the ABC compound after ionization according to the Example 7.

equations:

$$\frac{d[i_0]}{dt} = g(t) - k_{i_0 \rightarrow ABC^+}[i_0] - k_{i_0 \rightarrow AB^+}[i_0] \quad (\text{SI39})$$

$$\frac{d[ABC^+]}{dt} = +k_{i_0 \rightarrow ABC^+}[i_0], \quad (\text{SI40})$$

$$\frac{d[AB^+]}{dt} = +k_{i_0 \rightarrow AB^+}(1 - r_{AB^+ \leftrightarrow A^+}h(t))[i_0], \quad (\text{SI41})$$

$$\frac{d[A^+]}{dt} = +k_{i_0 \rightarrow AB^+}(r_{AB^+ \leftrightarrow A^+}h(t))[i_0]. \quad (\text{SI42})$$

These equations describe the dynamics shown in Figure SI28. Notice that in the absence of the perturbing pulse, the A^+ signal is zero. This is changed by the presence of the disrupting pulse as is plotted in Figure SI29, illustrating simulation of disruptive probing measurement. The fitting of the AB^+ and A^+ pump-probe signal presented in Figure SI30 reveals the fragmentation rates corresponding to the i_0 dynamics. Importantly, the ABC^+ channel is not affected.

Although this is only a model situation for a disruptive probing measurement, it also illustrates that the signals of different ion species, which the pump-probe signal shows a correlation, do not necessarily correspond to the topology of the original dynamics. In contrast, the described model scenarios support that the dynamical observations revealed by the disruptive probing technique are inherently connected to the original dynamics of the system.

I. Summary

The simple examples discussed illustrate how pump-probe disruptive probing measurements can yield

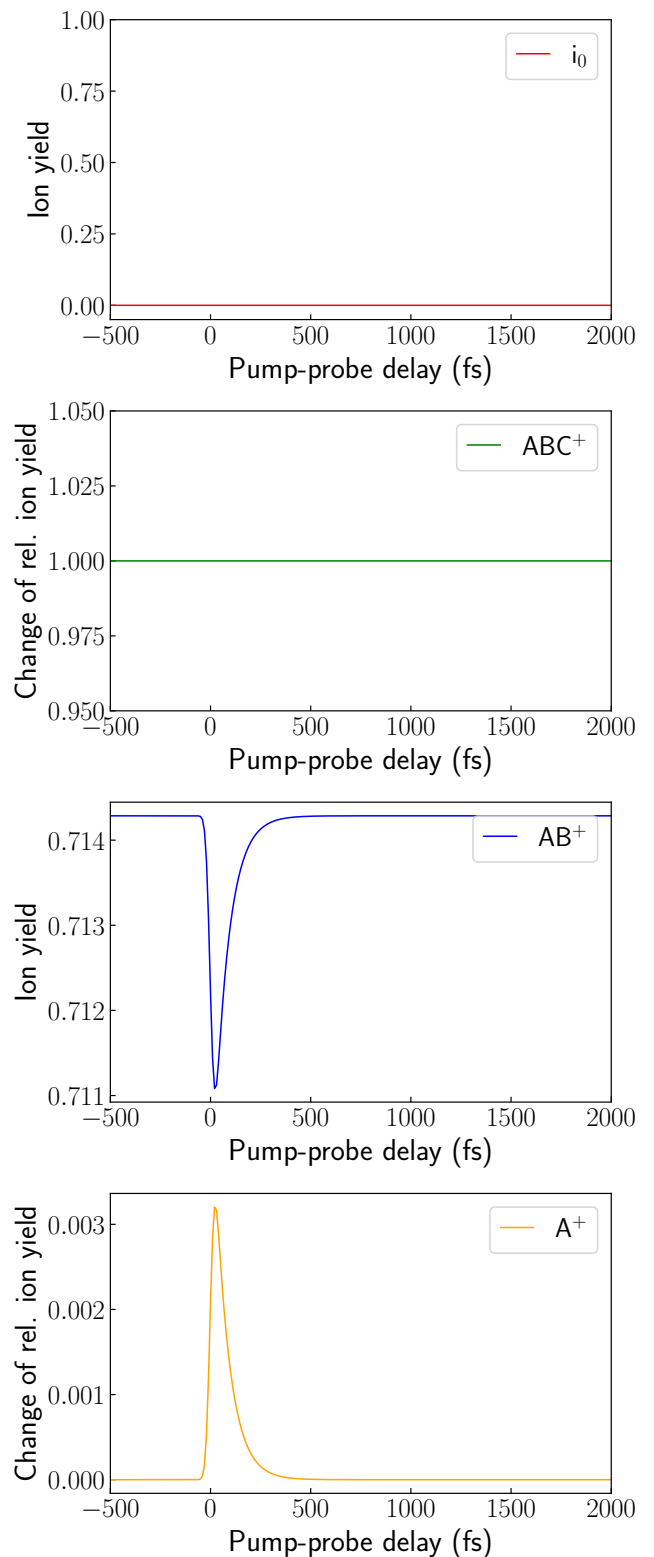


FIG. SI29. Simulated disruptive probing measurement in case of Example 7.

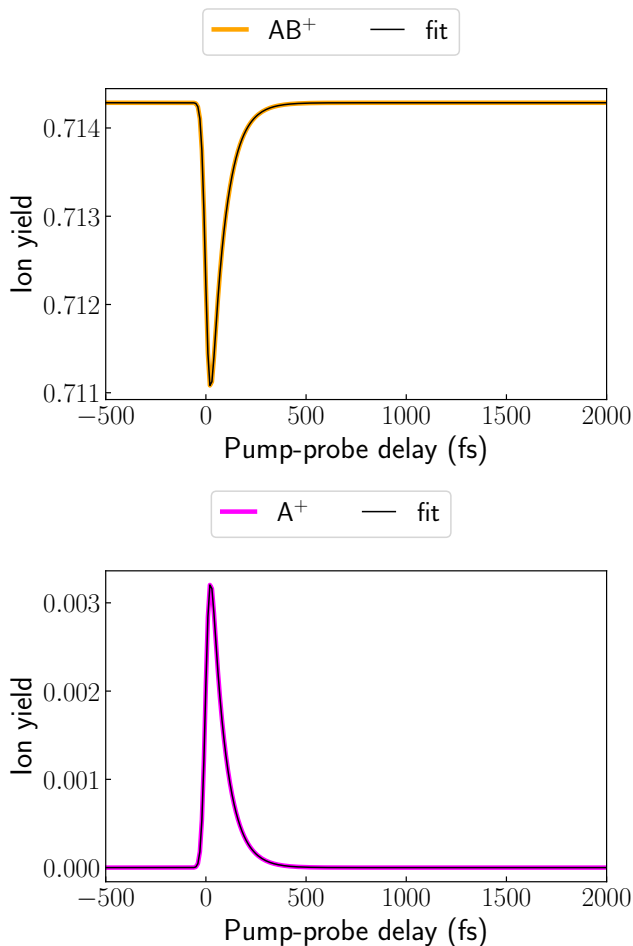


FIG. SI30. Fitted simulated signal dependences of AB^+ , and A^+ ion from Example 7.

markedly different results, depending on the topology of the system under study and the nature of the induced coupling changes.

In simple terms, the ansatz based on differential equations for describing disruptive probing experiments models the probe-induced, time-dependent changes in the ongoing dynamics. These changes can manifest as enhancements or diminutions of rate constants, the induction of new reaction pathways, or fragmentation into new ion products. Various mechanisms may be responsible for these effects, such as Stark coupling, rovibrational excitation, or Raman transitions. Accurately describing these processes in detail is extremely challenging and currently beyond our capabilities.

Nevertheless, the observed dynamics in pump-probe signals can provide a broad overview of the ongoing, unperturbed fragmentation processes. The models presented here can be particularly useful for an initial interpretation of pump-probe data and for preliminary discussion before engaging in more advanced molecular dynamics simulations.

J. Kinetic simulation of the disruptive probing experiment

The fitting of the pump-probe data shown in Figure 3 in the main text reveals three significant dynamics features occurring on different timescales. Firstly, fast process with effective lifetime in the order of tenths of femtoseconds revealed for H_3O^+ , H_2O^+ . Secondly, the dynamics occurring with effective lifetime between 200-400 fs for H_3O^+ , H_2O^+ , OH^+ , and O^+ . And lastly, slow dynamics of $(\text{H}_2\text{O})_2^+$ and H^+ in picosecond timescale.

Under our experimental condition, we can expect that the most of the singly ionized $(\text{H}_2\text{O})_2$ are occupying ground and the first excited state. In paper by Svoboda *et al.* [27], their simulation revealed that singly ionized water dimer in the first two electronic states should firstly proceed through proton transfer in tenths of femtoseconds leading to the creation of ion-radical pair $[\text{H}_3\text{O}^+ \cdots \text{OH}]$. Subsequently, this is either stabilized or leads to $\text{H}_3\text{O}^+ + \text{OH}$ fragmentation on the timescale of hundreds of femtoseconds.

The observed timescales of the first two features in the experimental data are in good agreement with the reported theory [27]. On the contrary, we would expect similar features observed not only in the H_3O^+ , H_2O^+ , OH^+ , and O^+ pump-probe signals, but also in $(\text{H}_2\text{O})_2^+$, which is not the case. Here we describe a model of disruptive probing experiment, which should explain the discrepancy.

The dynamics according to the Svoboda *et al.* is shown in Figure SI31 A. The differential equations describing the

scenario are written as

$$\frac{d[i_0]}{dt} = g(t) - k_{i_0 \rightarrow \text{H}_3\text{O}^+ - \text{OH}} \cdot [i_0], \quad (\text{SI43})$$

$$\begin{aligned} \frac{d[\text{H}_3\text{O}^+ - \text{OH}]}{dt} = & + k_{i_0 \rightarrow \text{H}_3\text{O}^+ - \text{OH}} \cdot [i_0] \\ & - k_{\text{H}_3\text{O}^+ - \text{OH} \rightarrow \text{H}_3\text{O}^+} \cdot [\text{H}_3\text{O}^+ - \text{OH}] \\ & - k_{\text{H}_3\text{O}^+ - \text{OH} \rightarrow (\text{H}_2\text{O})_2^+} \cdot [\text{H}_3\text{O}^+ - \text{OH}], \end{aligned} \quad (\text{SI44})$$

$$\frac{d[(\text{H}_2\text{O})_2^+]}{dt} = + k_{\text{H}_3\text{O}^+ - \text{OH} \rightarrow (\text{H}_2\text{O})_2^+} \cdot [\text{H}_3\text{O}^+ - \text{OH}], \quad (\text{SI45})$$

$$\frac{d[\text{H}_3\text{O}^+]}{dt} = + k_{\text{H}_3\text{O}^+ - \text{OH} \rightarrow \text{H}_3\text{O}^+} \cdot [\text{H}_3\text{O}^+ - \text{OH}]. \quad (\text{SI46})$$

As it is discussed in the disruptive probing example cases described in Section SI3 A, no probe-pulse-induced enhancement, reduction of rate constant in the can lead to our experimental observation, i. e., no observation of the changes in the $(\text{H}_2\text{O})_2^+$ signal and activity in the H_2O^+ , OH^+ , and O^+ ion signal. Therefore, we must assume that the probing pulse is in fact causing a transition of the part of the $[\text{H}_3\text{O}^+ \cdots \text{OH}]$ particles, which are ongoing the dissociating pathway into the H_3O^+ signal (for the simplicity of the model we will omit the OH^+ and O^+ signal dependencies). This can be modelled via introducing a new reshuffling factor $r_{\text{H}_3\text{O}^+ \leftrightarrow \text{H}_2\text{O}^+}$ in Equation SI46 and adding a new equation for induced H_2O^+ population as

$$\begin{aligned} \frac{d[\text{H}_3\text{O}^+]}{dt} = & + k_{\text{H}_3\text{O}^+ - \text{OH} \rightarrow \text{H}_3\text{O}^+} \cdot (1 - r_{\text{H}_3\text{O}^+ \leftrightarrow \text{H}_2\text{O}^+}) \times \\ & \times [\text{H}_3\text{O}^+ - \text{OH}], \end{aligned} \quad (\text{SI47})$$

$$\begin{aligned} \frac{d[\text{H}_2\text{O}^+]}{dt} = & + k_{\text{H}_3\text{O}^+ - \text{OH} \rightarrow \text{H}_3\text{O}^+} \cdot r_{\text{H}_3\text{O}^+ \leftrightarrow \text{H}_2\text{O}^+} \times \\ & \times [\text{H}_3\text{O}^+ - \text{OH}]. \end{aligned} \quad (\text{SI48})$$

In Figure SI31 B-F, there are simulated resulting ion signal dependencies for disruptive probing experiment. We can observe that the dynamics in H_3O^+ and H_2O^+ are mutually compensating as the probing-pulse does not populate any ions and only transfers population from one to the other ion species. Interestingly, the applied model links our experimental observations with the simulations and support our assignment of the dynamics on the scale of tenths and hundreds of femtoseconds to population and subsequent fragmentation, respectively, of $[\text{H}_3\text{O}^+ \cdots \text{OH}]$ as is illustrated also in Figure SI31 F.

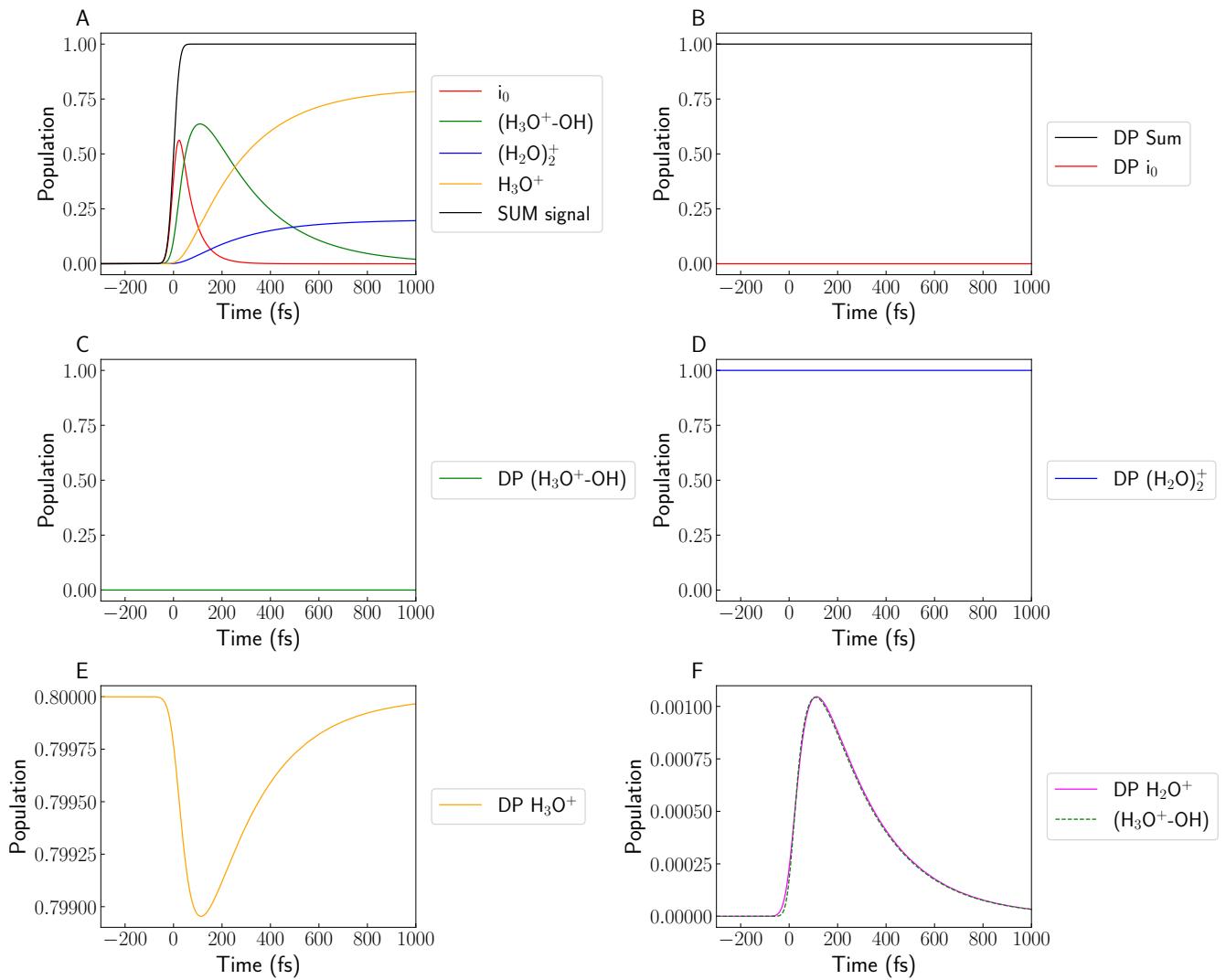


FIG. SI31. Numerical simulation of fragmentation of singly ionized water dimer dynamics from the ground and the first excited states using kinetics model described by Equation SI43-Equation SI48. (A) Unperturbed dynamics. (B-F) Simulation of the pump-probe signal dependencies in disruptive probing experiment for different ion species. (F) A comparison between the searched dynamics of $[\text{H}_3\text{O}^+ \cdots \text{OH}]$ (dashed green) with the simulated pump-probe signal dependence of H_2O^+ .

- [1] W. Jin, H. Bromberger, L. He, M. Johny, I. S. Vinklárek, K. Długołęcki, A. Samartsev, F. Calegari, S. Trippel, and J. Küpper, A versatile and transportable endstation for controlled molecule experiments, *Rev. Sci. Instrum.* **96**, 023305 (2025).
- [2] U. Even, The Even-Lavie valve as a source for high intensity supersonic beam, *Eur. Phys. J. Techn. Instrumen.* **2**, 17 (2015).
- [3] Y.-P. Chang, D. A. Horke, S. Trippel, and J. Küpper, Spatially-controlled complex molecules and their applications, *Int. Rev. Phys. Chem.* **34**, 557 (2015), arXiv:1505.05632 [physics].
- [4] S. Trippel, M. Johny, T. Kierspel, J. Onvlee, H. Bieker, H. Ye, T. Mullins, L. Gumprecht, K. Długołęcki, and J. Küpper, Note: Knife edge skimming for improved separation of molecular species by the deflector, *Rev. Sci. Instrum.* **89**, 096110 (2018), arXiv:1802.04053 [physics].
- [5] A. T. J. B. Eppink and D. H. Parker, Velocity map imaging of ions and electrons using electrostatic lenses: Application in photoelectron and photofragment ion imaging of molecular oxygen, *Rev. Sci. Instrum.* **68**, 3477 (1997).
- [6] H. Bromberger, C. Passow, D. Pennicard, R. Boll, J. Correa, L. He, M. Johny, C. Papadopoulou, A. Tul-Noor, J. Wiese, S. Trippel, B. Erk, and J. Küpper, Shot-by-shot 250 kHz 3D ion and MHz photoelectron imaging using Timepix3, *J. Phys. B* **55**, 144001 (2022), arXiv:2111.14407 [physics].
- [7] A. Al-Refaie, M. Johny, J. Correa, D. Pennicard, P. Svihra, A. Nomerotski, S. Trippel, and J. Küpper, PymePix: A Python library for SPIDR readout of Timepix3, *J. Instrum.* **14** (10), P10003, arXiv:1905.07999 [physics].
- [8] CFEL Controlled Molecule Imaging, PymePix, Code repository, URL: <https://gitlab.desy.de/CMI/CMI-public/pymepix> (2024).
- [9] B. Jochim, L. DeJesus, and M. Dantus, Ultrafast disruptive probing: Simultaneously keeping track of tens of reaction pathways, *Rev. Sci. Instrum.* **93**, 033003 (2022).
- [10] K. Schnorr, M. Belina, S. Augustin, H. Lindenblatt, Y. Liu, S. Meister, T. Pfeifer, G. Schmid, R. Treusch, F. Trost, P. Slavíček, and R. Moshhammer, Direct tracking of ultrafast proton transfer in water dimers, *Sci. Adv.* **9**, eadg7864 (2023).
- [11] J. C. Tully, Molecular dynamics with electronic transitions, *J. Chem. Phys.* **93**, 1061 (1990).
- [12] T. Shiozaki, BAGEL: Brilliantly Advanced General Electronic-structure Library, *WIREs Computational Molecular Science* **8**, e1331 (2018).
- [13] M. Ceriotti, G. Bussi, and M. Parrinello, Langevin equation with colored noise for constant-temperature molecular dynamics simulations, *Phys. Rev. Lett.* **102**, 020601 (2009), arXiv:0812.1168.
- [14] M. Ceriotti, G. Bussi, and M. Parrinello, <http://gle4md.org/>.
- [15] A. D. Boese and J. M. L. Martin, Development of density functionals for thermochemical kinetics, *J. Chem. Phys.* **121**, 3405 (2004).
- [16] G. W. T. M. J. Frisch H. B. Schlegel, G. E. Scuseria, M. A. Robb, J. R. Cheeseman, G. Scalmani, V. Barone, G. A. Petersson, H. Nakatsuji, X. Li, M. Caricato, A. Marenich, J. Bloino, B. G. Janesko, R. Gomperts, B. Mennucci, H. P. Hratchian, J. V. Ortiz, A. F. Izma, Gaussian 09 (2013).
- [17] P. Slavíček, M. Ončák, D. Hollas, and O. Svoboda, Abin (2020).
- [18] H.-J. Werner, P. J. Knowles, G. Knizia, F. R. Manby, and M. Schütz, Molpro: a general-purpose quantum chemistry program package, *WIREs Comput Mol Sci* **2**, 242 (2012).
- [19] H.-J. Werner, P. J. Knowles, P. Celani, W. Györfly, A. Hesselmann, D. Kats, G. Knizia, A. Köhn, T. Korona, D. Kreplin, R. Lindh, Q. Ma, F. R. Manby, A. Mitrushenkov, G. Rauhut, M. Schütz, K. R. Shamasundar, T. B. Adler, R. D. Amos, S. J. Bennie, A. Bernhardsen, A. Berning, J. A. Black, P. J. Bygrave, R. Cimiraglia, D. L. Cooper, D. Coughtrie, M. J. O. Deegan, A. J. Dobyn, K. Doll, M. Dornbach, F. Eckert, S. Erfort, E. Goll, C. Hampel, G. Hetzer, J. G. Hill, M. Hodges, T. Hrenar, G. Jansen, C. Köppl, C. Kollmar, S. J. R. Lee, Y. Liu, A. W. Lloyd, R. A. Mata, A. J. May, B. Mussard, S. J. McNicholas, W. Meyer, T. F. Miller III, M. E. Mura, A. Nicklass, D. P. O'Neill, P. Palmieri, D. Peng, K. A. Peterson, K. Pflüger, R. Pitzer, I. Polyak, M. Reiher, J. O. Richardson, J. B. Robinson, B. Schröder, M. Schwall, T. Shiozaki, M. Sibaev, H. Stoll, A. J. Stone, R. Tarroni, T. Thorsteinsson, J. Toulouse, M. Wang, M. Welborn, and B. Ziegler, Molpro, 2015.1 , a package of ab initio programs (2015).
- [20] I. S. Vinklárek, H. Bromberger, N. Vadassery, W. Jin, J. Küpper, and S. Trippel, Reaction pathways of water dimer following single ionization, *J. Phys. Chem. A* **128**, 1593 (2024), arXiv:2308.08006 [physics].
- [21] Z.-H. Loh, G. Doumy, C. Arnold, L. Kjellsson, S. H. Southworth, A. Al Haddad, Y. Kumagai, M.-F. Tu, P. J. Ho, A. M. March, R. D. Schaller, M. S. Bin Mohd Yusof, T. Debnath, M. Simon, R. Welsch, L. Inhester, K. Khalili, K. Nanda, A. I. Krylov, S. Moeller, G. Coslovich, J. Koralek, M. P. Minitti, W. F. Schlotter, J.-E. Rubensson, R. Santra, and L. Young, Observation of the fastest chemical processes in the radiolysis of water, *Science* **367**, 179 (2020).
- [22] S. Li, L. Lu, S. Bhattacharyya, C. Pearce, K. Li, E. T. Nienhuis, G. Doumy, R. D. Schaller, S. Moeller, M.-F. Lin, G. Dakovski, D. J. Hoffman, D. Garratt, K. A. Larsen, J. D. Koralek, C. Y. Hampton, D. Cesar, J. Duris, Z. Zhang, N. Sudar, J. P. Cryan, A. Marinelli, X. Li, L. Inhester, R. Santra, and L. Young, Attosecond-pump attosecond-probe x-ray spectroscopy of liquid water, *Science* **383**, 1118 (2024).
- [23] I. Vinklárek, M. Belina, H. Bromberger, Á. C. Fernandez, S. Trippel, P. Slavíček, and J. Küpper, (2025), in preparation.
- [24] D. M. Chipman, Hemibonding between water cation and water, *J. Phys. Chem. A* **120**, 9618 (2016).
- [25] A. Iguchi, A. Singh, S. Bergmeister, A. A. Azhagesan, K. Mizuse, A. Fujii, H. Tanuma, T. Azuma, P. Scheier, S. Kuma, and A. F. Vilesov, Isolation and Infrared Spectroscopic Characterization of Hemibonded Water Dimer Cation in Superfluid Helium Nanodroplets, *J. Phys. Chem. Lett.* **14**, 8199 (2023).
- [26] S. Hartweg, G. A. Garcia, and L. Nahon, Photoelectron spectroscopy of the water dimer reveals unpredicted vibrational structure, *J. Phys. Chem. A* **125**, 4882 (2021).
- [27] O. Svoboda, D. Hollas, M. Ončák, and P. Slavíček, Reaction selectivity in an ionized water dimer: Nonadiabatic

ab initio dynamics simulations, *Phys. Chem. Chem. Phys.*
15, 11531 (2013).